

UCLA

UCLA Previously Published Works

Title

Fly Feature Detectors Show Contrast Invariance, Omni-Directionality, Velocity Constancy, and Octopaminergic Loss of Background Motion Suppression

Permalink

<https://escholarship.org/uc/item/76t6k2f8>

Authors

Staedele, Carola
Keles, Mehmet
Mongeau, Jean-Michel
[et al.](#)

Publication Date

2020

DOI

10.2139/ssrn.3523357

Peer reviewed

1 **Non-canonical receptive field properties and neuromodulation of feature** 2 **detecting neurons in flies**

3 Carola Städele^{1,2}, Mehmet F. Keleş^{1,3}, Jean-Michel Mongeau^{1,4}, Mark A. Frye^{1*}

4 ¹ Department of Integrative Biology and Physiology, University of California Los Angeles, Los
5 Angeles, CA 90095-7239, United States

6 ² Present address: School of Biological Sciences, Illinois State University, Normal, IL 61790-
7 4120, United States

8 ³ Present address: Department of Neurology, Johns Hopkins University, Baltimore, MD 21205,
9 United States

10 ⁴ Present address: Department of Mechanical Engineering, Pennsylvania State University,
11 University Park, PA 16802, United States

12 * Lead contact: frye@ucla.edu

13 **SUMMARY**

14 Several fundamental aspects of motion vision circuitry are prevalent across flies and mice. Both
15 taxa segregate ON and OFF signals. For any given spatial pattern, motion detectors in both
16 taxa are tuned to speed, selective for one of four cardinal directions, and modulated by
17 catecholamine neurotransmitters. These similarities represent conserved, canonical properties
18 of the functional circuits, and computational algorithms for motion vision. Less is known about
19 feature detectors, including how receptive field properties differ from the motion pathway, or
20 whether they are under neuromodulatory control to impart functional plasticity for the detection
21 of salient objects from a moving background. Here, we investigated 19 types of putative feature
22 selective lobula columnar (LC) neurons in the optic lobe of the fruit fly *Drosophila melanogaster*
23 to characterize divergent properties of feature selection. We identified LC12 and LC15 as
24 feature detectors. LC15 encodes moving bars, whereas LC12 is selective for the motion of
25 discrete objects, mostly independent of size. Neither is selective for contrast polarity, speed, or
26 direction, highlighting key differences in the underlying algorithms for feature detection and
27 motion vision. We show that the onset of background motion suppresses object responses by
28 LC12 and LC15. Surprisingly, the application of octopamine, which is released during flight,
29 reverses the suppressive influence of background motion, rendering both LCs able to track
30 moving objects superimposed against background motion. Our results provide a comparative
31 framework for the function and modulation of feature detectors and new insights into the
32 underlying neuronal mechanisms involved in visual feature detection.

33

34 **KEYWORDS**

35 object vision; motion vision; visual processing; octopamine; lobula columnar neurons; visual
36 projection neurons

37 INTRODUCTION

38 The adage "A picture is worth a thousand words" highlights the economy of visual information. A
39 commonplace visual function is the perception of the features that discriminate salient objects
40 from a complex background scene. Salient features can include color, contrast, shape, size,
41 orientation, texture, or relative motion. Feature-detecting visual projection neurons (VPNs)
42 encode and convey this information between brain areas and have been identified in a variety of
43 animals including frogs [1], feline cortex [2,3], mouse superior colliculus [4,5], zebrafish tectum
44 [6], the optic lobe of dragonflies, blowflies, hoverflies [7–10], and fruit flies [11–14]. The
45 seemingly ubiquitous presence of feature detecting VPNs in a wide variety of taxa emphasizes
46 the evolutionary pressure for this form of visual processing. Yet the computational structure,
47 connectivity, and modulation of feature detectors remain poorly understood by comparison to
48 the heavily investigated mechanisms for motion vision [15–17]. Comparisons between the two
49 could provide fundamental insights.

50 Motion vision seems to be a broadly conserved neural computation as evidenced by striking
51 similarities between flies and mammals including parallel neuronal circuits for computing the
52 movement of dark (OFF) edges and bright (ON) edges, and selectivity by individual cells for
53 motion in one of four orthogonal directions [18]. Due to these similarities, great strides have
54 been made in elucidating the circuits underlying these computations. Circuit connectivity,
55 however, cannot fully explain motion vision, as neither the mammalian nor insect visual system
56 is functionally 'hard-wired' [19,20]. The mammalian retina is richly innervated by
57 catecholaminergic neurons releasing dopamine, epinephrine, and norepinephrine [21]. In flies,
58 the analog of norepinephrine, octopamine, acts to increase the response gain and frequency
59 sensitivity of motion-detecting neurons as well as every upstream input tested to date [20].

60 In flies, numerous putative feature detecting VPNs have been identified in the fourth optic
61 ganglion, the lobula [12,22–25], including the lobula columnar neurons (LCs, ~20 types). Each
62 LC class comprises 20 to 200 columnar copies [12]. LC dendrites tile the visual field and the
63 synaptic terminals form discrete glomerular structures where retinotopy is lost [11,12,26].
64 Recent studies have begun to explore the functional properties of LC neurons and their
65 responsiveness to visual features such as looming, edge motion, and small object motion [11–
66 13,26–30], but the functional properties of many of these LCs, their selectivity for the visual
67 features that draw flies' attention, and whether they share conserved properties of motion vision,
68 remains unresolved.

69 Here, we initiated a functional screen of 17 LC and 2 lobula plate lobula columnar (LPLC)
70 neuron classes for physiological responses to visual stimuli that evoke robust tracking of a
71 vertical bar [31,32], avoidance of a small object [31,33,34], and smooth fixation of a drifting
72 wide-field panorama [35,36]. Upon identifying LC classes that responded vigorously to these
73 stimuli, we comprehensively analyzed the receptive field properties using stimulus parameters
74 that characterized defined circuits in the motion pathway. Finally, we test the hypothesis that
75 octopamine modulates visual response gain, similar to the motion pathway [37–39]. We found
76 that the receptive field properties and LC neuromodulation differ qualitatively from the canonical
77 properties of the motion pathway.

78 RESULTS

79 We use the terms ‘wide-field’ or ‘panoramic’ to refer to visual stimuli, such as periodic gratings,
80 that extend over the entire elevation and azimuth of our display to stimulate a large portion of
81 the visual field. The terms ‘object’ and ‘figure’ refer to stimuli that differ from the visual
82 background and only stimulate a small visual field. A vertical bar and a small square are objects.

83 ***Several LC types show responses to vertical bars and small objects***

84 We screened 19 identified types of VPNS [12,23,24] for visual responses to three classes of
85 visual stimuli we refer to as standard stimuli: a dark 8.8×8.8° small object, a dark 8.8×70°
86 vertical bar against a uniformly lit background, and periodic wide-field grating (period 17.6°). All
87 stimuli moved at 22°/s (grating temporal frequency 1.25Hz). These stimuli are shown to evoke
88 robust visuomotor behaviors in walking and flying flies [31,33,34]. The screen included 17 LC
89 neurons and 2 LPLC neurons. We exclusively used split-GAL4 driver lines because of their high
90 specificity for the respective class of neurons. Visually evoked GCaMP6f responses from head-
91 fixed flies were recorded using two-photon calcium imaging (Figure 1A). Stimuli were projected
92 onto a cylindrical arrangement of light-emitting diodes, and recordings were performed in the
93 right optic lobe (Figure 1B). We recorded population activity of a given LC type by imaging from
94 the axon terminals forming a glomerulus in the ventrolateral protocerebrum (VLP, Figure 1C,
95 S1B-C). Although this is a small stimulus set, we were surprised to find that only five out of the
96 19 screened LC types responded to the bar or small object stimuli (Figure 1D). LC15 responded
97 mainly to the vertical bar, LC12 and LC16 responded to both the bar and the small object, and
98 LC11 and LC26 responded only to the small object. None of the 17 LC and 2 LPLC types
99 showed strong responses to the wide-field grating.

100 Qualitatively, response profiles generated with solid dark objects agreed with experiments in
101 which we controlled for spatial luminance cues with randomly textured objects moving against a
102 similar random background – the object disappears if it stops moving (Figure S1A). Most tested
103 LC types showed similar responses to motion-defined objects (Figure S1A) and luminance-
104 defined objects (Figure 1D). LC16 and LC26, however, respond only to luminance-defined
105 objects. LC16, as well as LC4, LC6, and LPLC2, have been previously shown to be excited by a
106 looming solid disk, or a single edge of the disk [12–14,30]. LC10a responds to 10° square
107 objects [29], but our driver labels LC10b [12], which is not excited by small objects (Ines Ribeiro
108 personal communication). Because LC16 or LC26 did not generalize luminance- and motion-
109 defined objects, we did not explore these LC types further. LC12 has been explored previously,
110 but only with bar or edge stimuli [27], not small objects. LC11 has been comprehensively
111 described previously [11]. We therefore focused on LC12 and LC15, as well as novel results of
112 two experiments with LC11. We have addressed the following questions: 1) What are the
113 cellular inputs to LC12 and LC15, and what information is conveyed within the postsynaptic
114 dendrites? 2) Which visual features of an object do LC12 and LC15 respond to, and what are
115 the receptive field properties?

116 ***Presynaptic activity evoked by small object motion is localized to lobula layers 2/3***

117 Identifying the presynaptic inputs is crucial to understanding the mechanism for feature
118 detection by higher-order LC projection neurons. We devised a computational approach to

119 screen >3500 registered *Janelia* GAL4 driver lines [40] for neurons that arborize within lobula
120 layers 2 to 4, where LC12 and LC15 postsynaptic arbors are located. We focused on lines
121 originating in the medulla or lobula plate. The screen identified 300-400 candidate input lines,
122 and we selected roughly 50 lines to test for LC connectivity. Our screen included T2 and T3
123 neurons, which are shown to be highly sensitive to small objects and to innervate LC11 [41], as
124 well as T4 and T5 motion-detecting neurons [42]. Our screen most likely did not include Tm2,
125 Tm3, Tm4, or Tm9. To determine whether a candidate line is synaptically connected to one of
126 the LC neurons, we tested for anterograde trans-Tango labeling [43] of LC glomeruli that can be
127 readily identified by their shape and location in the VLP [25]. Unfortunately, none of the selected
128 lines labeled LC12 or LC15 glomeruli (data not shown), including T2, T3, T4, and T5 neurons,
129 which is noteworthy given the broad interest in these cells. These negative results suggest that
130 neither LC12 nor LC15 receive direct synaptic inputs from any of the T neurons and may
131 instead rely heavily on indirect innervation pathways. Near-future electron microscopy
132 reconstruction results identify direct LC input partners and indirect circuits.

133 Our failure to identify potential input neurons motivated us to revisit the distribution of pre- and
134 postsynaptic LC neuron arborizations across lobula layers. Prior immunohistochemical studies
135 indicate a layer-specific neuropharmacological organization in the lobula. Lobula layers 2 and 3,
136 for example, show enriched GABAergic signaling [44], and layers 1 and 4 seem to be enriched
137 with cholinergic structures [45]. Confirming work by Wu and colleagues [12], co-labeling with
138 DenMark and synaptotagmin (*syt.eGFP*) [46] revealed that LC12 has no presynaptic sites in the
139 lobula (Figure 2A). Postsynaptic arbors were mainly concentrated in lobula layers 2 and 4, with
140 sparse arbors in layer 3. Figure 2B summarizes the known arbor distribution for all LC neurons
141 identified by our screen responsive to both motion-defined and luminance-defined objects
142 (LC11, LC12, LC15, Figure 1D, S1A), plus two others that respond to luminance-defined solid
143 objects only (LC13, LC16, LC26, Figure 1D). Whereas the distribution of pre- and postsynaptic
144 arbors for each of these LC types is complex, only LC11, LC12, and LC13, which are generally
145 responsive to small moving objects, possess postsynaptic arbors within lobula layer 2 (Figure
146 2B). We thus tested the hypothesis that motion-defined small object signals are conveyed
147 selectively to lobula layer 2. We expressed synapse-localized GCaMP6s within a pan-neuronal
148 driver line (R57C10-GAL4) and imaged presynaptic calcium activity in the lobula evoked by our
149 three test stimuli. We compiled maximum intensity projections within a narrow strip orthogonal
150 to the layers of the lobula (Figure 2C). Figure 2D shows data from three out of ten flies.
151 Subtraction of the bar response profile from the object response revealed that in each
152 preparation the small object strongly activated layer 2 and, in many preparations, also layer 3
153 (Figure 2D and E, obj-bar, Figure S2). By contrast, we did not find consistent layer-specific
154 activation by the bar. Activation by the wide-field grating was restricted mainly to layer 1 (Figure
155 2F), which is innervated by columnar T5 motion detectors [12]. Notably, columnar medulla T2a
156 (misidentified in [41] as T2) innervates layers 2/3, and T3 neurons innervate layer 3 [22]. T2 and
157 T3 are both sensitive to ON and OFF flashes, selective for small objects, and show trans-Tango
158 labeling of LC11 [41], but not LC12 and LC15. Thus, if LC11, LC12, and LC15 pool from any
159 common upstream pathways, they are likely complex and indirect.

160 ***LC12 and LC15 are ON-OFF object motion detectors***

161 To better understand the visual properties of LC12 and LC15, we first tested contrast polarity
162 preferences by using an $8.8 \times 70^\circ$ bright and dark vertical bar that moved $22^\circ/\text{s}$ horizontally over
163 the display. Previous experiments showed that LC12 and LC15 responded strongly to this bar
164 size (Figure 1D). In both LCs, the time series of GCaMP6f responses were similar for the
165 brightest ON, and the darkest OFF bar (Figure 3A) and peak responses were not statistically
166 different from each other (Figure 3A'). Parameterizing the Weber contrast indicated that LC12
167 and LC15 are selective for high contrast, regardless of polarity (Figure 3B, B'). Neither LC12
168 and LC15 showed contrast polarity differences and are thus equally sensitive to bright or dark
169 objects.

170 LC11 has been shown to detect only small objects when they are moving [11]. We tested if
171 LC12 and LC15 show a similar motion selectivity by comparing GCaMP6f responses of a
172 moving dark bar ($8.8 \times 70^\circ$, $44^\circ/\text{s}$ velocity) to the appearance (OFF transient) and disappearance
173 (ON transient) of a static flicker. The temporal frequency of the ON and OFF transients of the
174 static flicker coincided with the edge transitions imposed by the moving bar. Our data reveals
175 that LC12 and LC15 are both movement detectors. Both the average time course of GCaMP6f
176 activity (Figure 3C) and the peak response amplitude (Figure 3C') indicate that LC12 and LC15
177 are significantly more responsive to a moving bar than to the flicker generated by its edges.

178 ***LC12 dendrites span more columns than its receptive field whereas LC15 dendrites span
179 fewer***

180 The relationship between dendritic span and receptive field size could inform structure-function
181 relationships. We, therefore, revisited LC12 and LC15 anatomy by performing multicolor
182 stochastic labeling of single LC neurons (MCFO-1, [47]) and counted how many lobula columns
183 are covered by the dendrites of individual cells (Figure 4A). Similar to results described by Wu
184 and colleagues [12], we found that the dendrites of individual LC12 neurons spanned on
185 average five columns in the anteroposterior axis (5.2 ± 1.2 columns) and three columns in the
186 dorsoventral axis (3.3 ± 0.7 columns, $N=9$ flies, >50 cells). Considering that each column
187 samples $\sim 5^\circ$ of the visual field, the LC12 dendritic span corresponds to $\sim 26 \times 16^\circ$. By contrast,
188 individual LC15 dendrites spanned on average five columns in the anteroposterior axis (5.3 ± 0.6
189 columns) and five columns in the dorsoventral axis (5.1 ± 0.9 columns, $N=11$ flies, >50 cells),
190 corresponding to $\sim 26 \times 25^\circ$.

191 We next sought to characterize the receptive field (RF) size of individual LC12 and LC15
192 neurons. We measured single-cell responses of individual LC neurons within the LC cluster by
193 recording calcium responses of individual neurites in the lobula (Figure 4B) in response to a 2.2°
194 dark bar displaced in 13° increments in each cardinal direction (see Star Methods). In short, the
195 $105 \times 66^\circ$ arena test area was binned into eight azimuthal and five elevation sampling bins
196 (Figure 4C). For all tested LC12 neurons, the RF of individual neurites was very small, on the
197 order of a single 13° sampling bin (Figure 4C). By contrast, the RF of individual LC15 neurites
198 comprised at least three bins in the vertical and horizontal direction (Figure 4D). To determine
199 the average RF size across animals, we spatially normalized to the bin that showed the
200 strongest calcium responses (bin 0 = RF center) and plotted the surrounding responses relative
201 to bin 0 (Figure 4C', D'). LC15 neurites with their RF occluded by the display boundary were

202 excluded from the analysis. RF sizes for both LC types were consistent within and across
203 animals. On average, LC12 receptive field was 13° or smaller (Fig 4C'), whereas LC15
204 receptive field was ~40° in the horizontal and vertical direction (Figure 4D'). RF centers for both
205 LCs were distributed across the visual field (Fig 4C'', D'').

206 The difference in RF size between LC12 and LC15 could explain why there are about 200
207 copies of LC12 neurons to sample the full visual field, by comparison to about 70 copies of
208 LC15 neurons. When comparing the RF sizes with the dendritic span, we found that individual
209 LC12 dendrites span about twice as many columns in the anteroposterior axis as the receptive
210 field (26×16° dendritic span versus 13×13° RF), suggesting that dendrites of individual LC12
211 neurons are overlapping by about 50% and might thereby receive spatial inhibition. We found
212 the opposite for LC15 in which individual LC15 dendrites cover only 60% of the RF (26×25°
213 dendritic span versus 40×40° RF).

214 ***LC12 is a speed-insensitive horizontal motion detector, while LC15 is a speed-insensitive*** 215 ***omni-directional motion detector***

216 Motion detectors show strong preferences for stimulus direction [3,42,48]. We tested whether
217 LC12 or LC15 show directional selectivity. From the data collected during the RF scan, we
218 extracted the maximum GCaMP6f responses of individual neurites to the movement of a 2.2°
219 wide dark bar in each of the four cardinal directions (22°/s velocity). We found that LC12
220 responded equally to motion in either direction along the horizontal axis (Figure 5A, top) but was
221 almost insensitive to motion in the vertical axis. The RF size and dendritic span of individual
222 LC12 neurons might explain this finding. Both are small in the vertical dimension. It seems
223 plausible that there is little vertical dendritic overlap between adjacent LC12 neurons, which
224 would explain why individual LC12 neurons are only responsive to a small spot (13°) along this
225 dimension. By contrast, LC15 appeared to be omnidirectional and showed the same response
226 amplitude to motion in all four directions (Figure 5A, bottom).

227 The velocity of behaviorally relevant signals is an essential parameter for behavioral control. An
228 object that approaches quickly elicits an escape response while a slow approaching object
229 might be ignored. We tested speed dependence in LC12 and LC15 by using an 8.8×70° dark
230 bar moving horizontally from front to back with velocities ranging from 22 to 132°/s. Average
231 peak calcium responses in both LC12 and LC15 were not statistically different across this speed
232 range (Figure 5B), which contrasts with LC11 that shows a monotonic increase in response
233 amplitude, peaking at 220°/s [41]. The flat velocity profile could reflect neuronal saturation
234 driven by high contrast stimuli. We noted, however, that although peak amplitude was
235 insensitive to speed, GCaMP6f response duration was correspondingly larger for slow motion
236 and shorter for fast motion (Figure 5C). Slower stimuli are displayed over a longer time than
237 faster stimuli.

238 ***LCs show complex combinations of spatial inhibition and spatial saturation***

239 Most of the visual stimuli used to this point comprised 8.8° wide vertical bars or small objects.
240 We next tested for object size tuning of both LCs. We recorded population activity from the
241 presynaptic glomerulus in response to objects of varying height and width. For LC12, GCaMP6f
242 response amplitude increased with object height and saturated for bars 35° or taller (Figure 6A,

243 top). By contrast, LC15 responses increased monotonically with object height and did not reach
244 a plateau (Figure 6A, bottom). Thus, neither LC12 nor LC15 appeared to be size tuned in the
245 vertical dimension, suggesting that there is no surround inhibition impinging upon the RF. The
246 decreased response latency of LC15 with bar height could reflect the spatial organization of the
247 receptive fields being pooled in the glomerulus, or instead, be due to taller objects moving
248 further into an asymmetric receptive field. Our data reject the latter conclusion because the
249 receptive fields are relatively symmetrical (Figure 4D, D'') and do not become asymmetrical in
250 the peripheral areas of the lobula. Since both LCs showed strong responses to bars, we used
251 this stimulus to test for width preference. Systematically varying bar width revealed some
252 peculiar differences between the two LCs. Peak amplitude responses by LC12 were rather flat
253 for increasing bar width, but the duration of the response increased (Figure 6B, top). By
254 contrast, LC15 showed classical size tuning in the horizontal dimension, with peak amplitude
255 responses for the smallest bars and decreasing to less than half maximum for bars 18° or wider
256 (Figure 6B, bottom).

257 The systematic increase in the temporal duration and dual peaks in GCaMP6f responses to
258 wide bars (Figure 6B) motivated us to examine whether signaling in the terminal glomerulus
259 reflected two discrete 'waves' of activity within the dendrites corresponding to the leading and
260 trailing edges of a wide bar. We recorded from single dendritic neurites in the lobula to bars of
261 two different widths (4.4° and 70°). For both LCs, the narrow bar generated a single GCaMP6f
262 peak, whereas the wider bar generated discrete full-amplitude responses to both the leading
263 and trailing edges (Figure 6C, C'). Equivalent response amplitude to the OFF and ON edges of
264 the dark bar support the lack of selectivity for contrast polarity in these LCs (Figure 3B, B'). The
265 narrow bar elicited half-maximum response duration on average 0.7 ± 0.2 s longer for LC12 (7
266 flies, 20 dendrites) and 0.6 ± 0.1 s longer for LC15 (7 flies, 19 dendrites) than the response to the
267 leading edge of the wide bar. This suggests that both LCs responded to the leading and trailing
268 edges of the 4.4° narrow bar, but the GCaMP6f decay kinetics effectively fused these dynamics.
269 In summary, we have found that both LC12 and LC15 show no clear height tuning but that LC15
270 showed the strongest responses to bars narrower than 8.8°. Table S1 summarizes all visual
271 response properties of LC12 and LC15.

272 ***Octopaminergic neuromodulation enables object detection against background motion***

273 A potent property of some feature detectors is their ability to distinguish object motion against
274 the background optic flow generated when the observer is moving [5,9,49,50]. For LC11,
275 however, the onset of background motion suppresses small object responses [41], implying that
276 this cell class is only effective for object motion detection when the animal is stationary. We
277 tested whether similar response suppression by background motion occurs in LC12 and LC15
278 by presenting an $8.8 \times 70^\circ$ dark bar moving at $44^\circ/\text{s}$ over a low contrast background grating. In
279 both LC12 and LC15, bar responses were rapidly and significantly suppressed by concomitant
280 background grating motion (Figure 7A, A').

281 Recent studies have shown that the baseline membrane potential and visually evoked
282 responses of visual neurons can be influenced by the animal's locomotor state [39,51]. On flight
283 initiation, the nervous system of *Drosophila* is flushed with the biogenic amine octopamine,
284 which increases the response gain of motion-sensitive neurons in the medulla and lobula plate

285 [20]. To test the hypothesis that octopamine modulates the function of LC12 and LC15, we bath-
286 applied the octopamine agonist chlordimeform [52] (CDM, 100 μ M) and repeated the previous
287 experiment. CDM application did not significantly alter either LC12 or LC15 responses to a dark
288 bar presented over a low contrast stationary grating (Figure 7B, bar only). To our surprise,
289 however, CDM application reversed the suppression of bar responses by superimposed
290 background grating motion. In CDM, LC12 mean response amplitude was restored to that
291 evoked by bar motion alone (Figure 7B, bar+bkg). Bar responses by LC15 were only partially
292 restored but were significantly larger in CDM than in the saline control (Figure 7B'). We found
293 qualitatively similar results for experiments in which wide-field motion was initiated midway
294 through a bar response, or for experiments in which we varied the direction of bar and
295 background motion (Figure S3). To test whether the influence of CDM is widespread among
296 feature detecting LCs, we repeated the experiment with LC11 using an 8.8° dark square object
297 moving at 44°/s over a background grating. CDM application had no significant influence on
298 object motion responses with a stationary grating, nor did CDM alter the fully suppressive effect
299 of wide-field grating motion on LC11 small-object responses (Figure 7C, C').

300 DISCUSSION

301 In addition to their selectivity for sophisticated features of moving stimuli such as small objects
302 or bars, lobula columnar projection neurons show RF properties and aminergic neuromodulation
303 that differ markedly from motion vision circuits, adding a layer of complexity to visual processes
304 that may be broadly shared across taxa.

305 ***Object detecting LCs are broadly indifferent to object contrast polarity, movement*** 306 ***direction and velocity***

307 In flies, as in mammals, photoreceptor signals are multiplexed into two parallel half-wave
308 rectified contrast polarity channels for ON and OFF edges [53–55]. These pathways culminate
309 with columnar motion detectors selective for moving ON edges (T4) and OFF edges (T5) [56].
310 Neither of the LCs tested here showed contrast polarity selectivity (Figure 3A, B). Interestingly,
311 the medulla columnar neurons T2a and T3 project to lobula layer 2/3 and innervate the small-
312 object selective motion detector LC11. LC12 and LC15 are similarly agnostic for contrast
313 polarity as LC11 [11], acting instead as full-wave rectifiers of luminance changes [41]. A
314 proposed elementary feature detector rectifies inputs for the temporal correlation of ON and
315 OFF sequences at a single point in space [57,58]. A visual computation dependent upon a
316 single spatial input would be directionally non-selective by definition. By contrast to individual
317 columnar T4 and T5 motion detectors that are selective for one of four orthogonal directions of
318 motion [56], columnar LC12 and LC15 neurons show no directional selectivity (Figure 5A),
319 similar to LC11 [11]. The peculiar structure of axial directional tuning in LC12 might indicate
320 strong orientation selectivity, which enhances directional selectivity in T4/T5 [59]. However,
321 GCaMP6f responses by LC12 to a static bar oriented orthogonal to its preferred motion axis
322 (Figure 3C, C') are weak by comparison to T4/T5.

323 For a fixed spatial pattern, motion detectors are speed tuned. When presented with a single-
324 pixel bar on a similar LED display over a similar speed range as used here, T4 motion detectors
325 show clear response tuning to the velocity of a periodic grating with peak responses at ~28°/s

326 [60]. By contrast, LC12 and LC15 show an even distribution of max $\Delta F/F$ responses between
327 22-132°/s (Figure 5B). Likewise, small target motion detectors (STMDs) of the hoverfly lobula
328 show broad velocity tuning, with spiking frequency constant between 20-120°/s [9].
329 Nevertheless, STMD neurons can provide unambiguous information about object velocity. The
330 number of spikes scales linearly with object speed in STMDs [61]. Similarly, the duration of
331 GCaMP6f responses by LC12 and LC15 diminish with increasing speed (Figure 5C), indicating
332 that total calcium accumulation and, therefore presynaptic release may scale with speed.

333 ***LC12 and LC15 show complex relationships between spatial dendritic span and receptive*** 334 ***field size***

335 To understand the lateral spread of visual signals, a comparison of the RF and dendritic spread
336 of a neuron is useful. The input dendrites of T4 and T5 neurons span at least seven columns in
337 a hexagonal array, equivalent to 15° of visual space [62], corresponding well with the 20°
338 functional RF [63]. By contrast, LC11 has a much larger dendritic span than RF [11]. LC12
339 dendrites sample roughly twice as many columns as the RF would predict, while LC15 dendrites
340 span only 60% (Figure 4C', D'). It would be tempting to speculate that size tuning by inhibition
341 requires columnar inputs surrounding the classical RF, which would be supported by the
342 exquisite size tuning in LC11 (strong surround inhibition). However, LC12 responses saturate
343 once the RF is filled (no surround inhibition), and LC15 shows horizontal size tuning (Figure 6B),
344 but its dendritic span undersamples the RF (Figure 4D'). Future work on subcellular synaptic
345 connectivity and transmitter identity will resolve these complexities.

346 ***LCs show qualitative functional shifts by neuromodulation***

347 Visual processing in insects is remarkably plastic and can be regulated by chemical
348 neuromodulators, cross-modal sensory inputs, and internal states [20]. Octopamine has long
349 been associated with homeostatic responses to the amplified metabolic and cell-energetic
350 demands of insect flight [64]. In the motion vision pathway, bath applied octopamine (or its
351 agonist chlordimeform [52]) increases the amplitude of visually evoked responses by medulla
352 interneurons, slightly shifts the frequency sensitivity of postsynaptic small-field T4/T5 motion
353 detectors, and increases the amplitude and shifts frequency sensitivity in wide-field motion
354 detectors of the lobula plate [38,39,65,66].

355 Octopamine seems to modulate neurons of the motion pathway quantitatively by increasing
356 visual response gain, but without changing RF size or other qualitative characteristics [65]. By
357 contrast, octopamine changes the qualitative structure of LC12 and LC15 responses by
358 enhancing object detection against a moving panorama (Figure 7). Recent work has revealed
359 striking effects of octopaminergic neuromodulation on behaviors driven by visual features.
360 *Drosophila melanogaster* instinctively avoid small moving objects in flight [33]. Yet, optogenetic
361 stimulation of octopaminergic neurons reverses object aversion to approach [34]. Signals from
362 looming detectors LC4 and LPLC2 are only transmitted to a pair of descending neurons
363 (DNp07, DNp10) when the animal is flying, or octopamine is bath applied [51]. How LC12 and
364 LC15 participate in object behaviors in *Drosophila* is unknown, yet octopamine mediated object
365 detection is reminiscent of the dragonfly lobula STMD neuron CSTMD1 [57,67], which responds
366 to a small contrasting target even it is presented against a moving panoramic background [68].
367 Future work can uncover the presynaptic inputs, visual processing algorithms, and integration

368 sites with the motion vision pathway to illuminate the mechanisms underlying the rich repertoire
369 of visual behaviors that flies possess.

370 **ACKNOWLEDGEMENTS**

371 This work was supported by the National Institutes of Health grant R01-EY026031 to M.A.F. We
372 thank Volker Hartenstein for use of his laboratory microscopy resources, and Ben Hardcastle for
373 technical assistance and Fernando Vonhoff for helpful discussion.

374 **AUTHOR CONTRIBUTIONS**

375 C.S. designed experiments, collected LC imaging screen data, performed imaging and
376 immunohistochemistry experiments, analyzed data, prepared figures, and wrote the paper;
377 M.F.K. designed experiments, provided code and reagents, and edited the paper; J.M.M.
378 collected LC imaging screen data; M.A.F. acquired funding, conceived the scope of work,
379 designed experiments, provided supervision, and wrote the paper.

380 **DECLARATION OF INTERESTS**

381 The authors declare no competing interests.

382 **FIGURE CAPTIONS**

383 **Figure 1. Few lobula columnar neurons respond to vertical bars or small objects. (A)**
384 Two-photon calcium imaging. Head-fixed flies were presented with visual stimuli from a
385 surrounding LED display. **(B)** Recordings were made from the right optic lobe. **(C)** Schematic of
386 *Drosophila* optic lobe neuropils, with the lobula highlighted in red. **(D)** Mean (+/- SD shading)
387 glomerular GCaMP6f responses by LC neuron types to a moving solid 8.8x8.8° dark object, an
388 8.8x70° dark bar and wide-field grating (17.6° period). Visual stimuli are depicted at the top and
389 moved from contra- to ipsilateral at 22°/s. Dashed lines indicate passing across the arena
390 midline (0°). N = at least 5 flies for each LC type. Re=retina, La=lamina, Me=medulla,
391 LoP=lobula plate, Lo=lobula, VLP= ventrolateral protocerebrum. See also responses to motion
392 defined stimuli in Figure S1.

393 **Figure 2. Presynaptic neuronal responses to small object motion is observed in lobula**
394 **layer 2/3. (A)** Single plane confocal images of the anterior view of flies expressing DenMark and
395 synaptically-tethered GFP (UAS-DenMark; UAS-syt.eGFP). Neuropil was labeled with anti-
396 Bruchpilot antibody nc82 (gray). **(B)** Summary diagram of pre- and postsynaptic (dendritic)
397 arbors of LC neuron types that showed responses to small objects and bars, reconstructed from
398 DenMark and synaptotagmin staining. **(C-F)** Layer-specific small object input to the lobula. **(C)**
399 Single plane confocal image illustrating the recording site (colored) used to determine layer
400 specific lobula input. **(D)** Mean activity images of sytGCaMP6s expressed in a pan neuronal
401 driver (R57C10-GAL4) in response to a 8.8° object (obj.), a 8.8x70° bar, and 17.6° wide-field
402 grating (WF) from three representative flies (see data from all flies in Figure S2). Approximate
403 layer boundaries are indicated with dashed lines, constructed from high resolution images
404 (gray). Schematics indicate innervated layers as filled circles. Obj-bar and bar-WF shows
405 subtracted mean calcium response of the corresponding visual stimuli. **(E-F)** Layer specific input

406 to the lobula for all tested flies (N=10), as maximum mean activity (norm $\Delta F/F$) for each layer,
407 normalized to the maximum response within a given fly.

408 **Figure 3. LC12 and LC15 are ON-OFF object motion detectors.** (A) Mean GCaMP6f signals
409 (+/- SD shading) of LC12 and LC15 glomeruli in response to a bright (ON, orange) and dark
410 (OFF, black) bar ($8.8 \times 70^\circ$, moved at $22^\circ/s$). (A') Pairwise comparison of LC12 and LC15
411 OFF/ON maximum $\Delta F/F$ responses. Circles represent the mean of three repetitions of individual
412 animals, diamonds present the mean across all animals tested +/-SD. n.s. = not significant.
413 LC12: N=7 flies, LC15: N=8 flies. Statistics: paired t-test, LC12: $t(6) = 2.74$, $p = 0.064$, LC15:
414 $t(7) = 2.15$, $p = 0.069$. (B) Mean GCaMP6f signal of LC12 and LC15 glomeruli in response to
415 varying contrast bars ($8.8 \times 70^\circ$, $22^\circ/s$). (B') Comparison of LC12 and LC15 contrast selectivity.
416 Fill color of circles represents the bar luminance. Circles represent the mean +/-SD across all
417 animals. LC12: N=7 flies, LC15: N=8 flies. (C) Mean GCaMP6f glomeruli signals in response to
418 an $8.8 \times 70^\circ$ stationary flickering bar (green) appearing and disappearing at $+26^\circ$ on the display,
419 and the same bar moving with $44^\circ/s$ (black). LC12: N=12 flies, LC15: N=10 flies. (C') Pairwise
420 comparison of maximum peak responses of the data shown in (C). Circles represent individual
421 animals, diamonds depict the mean +/-SD. Statistics: paired t-test. LC12: $t(11) = 5.97$, $p =$
422 $9.35e-05$, LC15: $t(9) = 7.47$, $p = 3.81e-05$. See summary in Table S1.

423 **Figure 4. LC15 has a larger receptive field than LC12.** (A) Spatial distribution of LC12 and
424 LC15 arbors in the lobula. Single layer confocal images of stochastically labeled LC12 and
425 LC15 neurons (MCFO-1). Lobula columns indicated with dashed lines. D=dorsal, V=ventral,
426 M=medial, L=lateral, A=anterior, P=posterior. Scale bars, $25 \mu m$. (B) Single confocal plane
427 image of LC12 in the anterior view illustrating the recording site (dashed rectangle). (B')
428 Representation of visual stimuli used to scan the RF. The gray highlighted region of the display
429 was divided into 13.2° spaced bins within which a 2.2° dark bar stimulus was moved in all four
430 cardinal directions (up, down, left, right, $22^\circ/s$). (C, D) Single cell RF mapping from
431 representative flies. Left: Single neurite regions of interest overlaid on single plane two-photon
432 images. Scale bars, $5 \mu m$. Right: Multiplied calcium traces from representative LC12 and LC15
433 recordings arranged in a grid corresponding to (B'). (C', D') Mean functional RF size of all tested
434 flies, where bin # 0 represents the RF center. Histograms show the mean peak GCaMP6f
435 responses +/-SD for each normalized bin. LC12: N=8 flies, n=26 neurites, LC15: N=5 flies, n=20
436 neurites. Purple sphere indicates the average anatomical RF depicted as retinal ommatidia
437 corresponding to individual lobula columns. (C'', D'') Spatial distribution of RF centers of the
438 cells included in C' and D' arranged in a grid corresponding to (B). Dots represent individual
439 cells. See summary in Table S1.

440 **Figure 5. Neither LC12 nor LC15 are selective for stimulus direction or velocity.** (A)
441 Directional tuning analysis of the data shown in Figure 4C'-D'' Each dot represents the
442 maximum $\Delta F/F$ response of individual cells to a 2.2° dark bar stimulus moving in the four
443 cardinal directions ($22^\circ/s$ velocity). Bars indicate mean. LC12: N=8 flies, n=26 neurites, LC15:
444 N=5 flies, n=20 neurites. (B) Responses of LC12 and LC15 to an $8.8 \times 70^\circ$ dark bar moving at
445 $22-132^\circ/s$. Circles represent mean +/-SD. LC12: N=12 flies, LC15: N=10 flies. Responses were
446 not statistical significant from each other (one way ANOVA, LC12: LC12: $F(5,66)=0.561$,
447 $p=0.729$, LC15: $F(5,54)=0.175$, $p=0.970$). (C) Thin gray traces represent GCaMP6f responses

448 of individual flies (three trials averaged), and thick colored traces show the mean across all
449 animals tested to a 8.8x70° dark bar moving at 22-132°/s. LC12: N=12 flies, LC15: N=10 flies.
450 See summary in Table S1.

451 **Figure 6. LC12 is an edge detector with spatial saturation and LC15 is a narrow-bar**
452 **detector with spatial inhibition. (A-B)** Mean maximum glomerular calcium responses to (A)
453 varying bar height (B) and varying bar width (velocity: 22°/s). Left: Mean responses +/-SD for
454 LC12 (N=9 flies) and LC15 (N=10 flies). Vertical dashed lines indicate receptive field (RF) size.
455 (C) Representative dendritic responses of individual neurites to a 4.4° (orange) and 70° (blue)
456 wide bar. (C') Pairwise comparison of maximum responses across animals. Circles represent
457 single cells, diamonds depict mean responses +/-SD. n.s. = not significant. LC12: N=7 flies,
458 n=20 dendrites, LC15: N=7 flies, n=19 dendrites. Statistics: paired t-test, LC12: 4.4°: t(19) =
459 16.39, p = 1.15e-12, 70°: t(19) = -2.98, p = 0.054; LC15: 4.4°: t(18) = 12.451, p = 2.78e-10, 70°:
460 t(18) = 2.32, p = 0.062. Scale bars, 5 µm. See summary in Table S1.

461 **Figure 7. Octopaminergic modulation enables object detection against background**
462 **motion in LC12 and LC15 but not in LC11. (A)** Glomerular GCaMP6f responses of LC12 and
463 LC15 in response to an 8.8x70° dark bar moving contra- to ipsilateral with 44°/s over a
464 stationary background (bar only) and both bar and wide-field background moving 44°/s from
465 contra- to ipsilateral (bar + bkg). Gray traces represent individual flies while black traces show
466 the mean across all animals tested. Time of bar and background movement is indicated with
467 solid horizontal bars. Dashed vertical lines indicate the time when visual stimuli passed the
468 arena midline. LC12: N=7 flies, LC15: N=8 flies. (A') Pairwise comparison of maximum $\Delta F/F$ of
469 traces shown in A. Circles represent individual flies while diamonds show mean +/- SD. Paired
470 t-test, LC12: t(6) = 5.47, p = 0.0009, LC15: t(7) = 14.97, p = 1.42e-06. (B, B') Same as A but
471 mean GCaMP6f responses (+/- SD shaded) for LC12 and LC15 in control condition (saline,
472 black) and in the presence of 100 µM CDM (magenta). LC12: N=7 flies, LC15: N=8 flies. Paired
473 t-test, LC12: t(6) = -3.03, p = 0.019, LC15: t(7) = -10.47, p = 1.58e-05. (C, C') Same as B but
474 LC11 responses to an 8.8x8.8° dark small object. N=8 flies, paired t-test, LC11: t(7) = -0.61, p =
475 0.56. See data from both horizontal stimulus directions in Figure S3.

476 STAR METHODS

477 RESOURCES AVAILABILITY

478 *Lead contact*

479 Further information and requests for resources and reagents should be directed to and will be
480 fulfilled by the Lead Contact, Mark Frye (frye@ucla.edu).

481 *Materials availability*

482 This study did not generate new unique reagents.

483 *Data and Code Availability*

484 The datasets and MATLAB analysis code used for this study are available at Mendeley Data
485 (doi: 10.17632/ssgpb4wmh9.1).

486 **EXPERIMENTAL MODEL AND SUBJECT DETAILS**

487 ***Fly stocks and handling***

488 Calcium imaging and anatomy experiments were performed with female *D. melanogaster* flies
489 3-5 days after eclosion, maintained under standard conditions (25°C, 30-50% humidity, 12h
490 light/dark cycle, standard cornmeal food). To genetically target LC neurons we exclusively used
491 split-GAL4 [69,70] driver lines because of their high specificity for the respective class of
492 neurons. Fly driver lines were crossed with fly effector lines (Key Resources Table, and Table
493 S1), and the progeny was used for experiments.

494 ***LC12 and LC15 driver lines***

495 OL0042B [12] was used as a driver line to genetically target LC15. Two different driver lines
496 were used to genetically target LC12: OL0007B and OL0008B [12]. Both LC12 driver lines are
497 highly specific and show no off-target labeling in 3-5 days old flies in the lobula or the
498 ventrolateral protocerebrum (VLP) where LC12 axons terminate in an optic glomerulus. We
499 compared calcium responses of OL0007B and OL0008B and found no statistically significant
500 difference in response amplitude or dynamics. For experiments where LC12 responses are
501 recorded but not manipulated (as in our study) both lines can be used interchangeably. We
502 found for flies that are older than ~14 days, the OL0007B driver showed weak labeling in LC10
503 as well. Calcium imaging experiments were performed using either OL0007B or OL0008B but
504 all anatomical data were collected using only OL0008B.

505 **METHOD DETAILS**

506 ***Solutions***

507 *D. melanogaster* saline was composed of (in mM): 103 NaCl, 3 KCl, 1.5 CaCl₂, 4 MgCl₂, 26
508 NaHCO₃, 1 NaH₂PO₄, 10 trehalose, 10 glucose, 5 TES, 2 sucrose, adjusted to 273–275 mOsm,
509 pH 7.3. For pharmacological experiments, agonists were prepared from concentrated stock
510 solutions immediately before the experiment. Stock solutions were stored at –20°C in small
511 quantities and diluted in *D. melanogaster* saline to the final concentration. Chlordimeform
512 (Sigma-Aldrich, 31099) was prepared as a 1mM stock solution in ultrapure water (18.3 MΩ,
513 Millipore) and used at a final concentration of 100μM. Measurements were taken after 15min
514 wash in.

515 ***Fly preparation for optical imaging***

516 Female flies were anesthetized at 4°C on a cold plate and mounted to a 3D printed fly holder
517 (modified from [71]) using ultraviolet glue (Dreve Fotoplast gel, Audiology Supplies, 44811). The
518 fly's legs were immobilized with low melting point beeswax to eliminate interference with
519 recordings and visual stimulation. Fine forceps (Dumont, #5SF, Fine Science Tools) were used
520 to remove the cuticle on the posterior surface of the fly's head to expose the right optic lobe in
521 the region of the lobula and VLP (Fig 1B, 1C).

522 ***Two-photon optical imaging***

523 During two-photon imaging the brain was continuously perfused with fly extracellular saline at
524 1.5 ml/min via a computer-controlled system (VC-6, Warner Instruments). Bath temperature was
525 kept at 20°C with an inline-solution heater (SC-20, Warner Instruments) and a temperature

526 controller (TC-324, Warner Instruments). LC neurons were imaged at 920nm using a
527 Ti:Sapphire pulse laser (Coherent, Santa Clara, CA) controlled by SlideBook (Version 6, 3i,
528 Boulder, CO). We imaged with a 20x water-immersion objective (W Plan Achromat, 1.0 DIC,
529 Zeiss) with three layers of blue filter (Indigo, Rosco, No. 59) to reduce bleed-through from the
530 LED arena to the photomultipliers. Single plane images were taken at 10 frames/s with each
531 frame at a x-y pixel resolution ranging from 150x256 to 168x212 and 0.2 to 0.3 μm pixel
532 spacing. To record population responses of a given LC type, GCaMP6f responses were
533 recorded in the LC output glomeruli where all terminals merge together. To record activity of
534 single LC neurons, GCaMP6f responses were measured from individual dendritic neurites in the
535 lobula.

536 **Visual Stimulation**

537 Visual stimuli during two-photon imaging were presented on a cylindrical LED arena [72]. The
538 arena was composed of 4 rows and 12 columns of 8x8 LED dot matrix panels (470nm,
539 Dongguan Houke Electronic Co., 12088-AB). The LED display covered +/-108° of the visual
540 field in the horizontal, and +/-35° in the vertical dimension. Each pixel subtended 2.2° on the
541 fly's retina at the visual equator. Stimuli were generated and controlled using custom MATLAB
542 scripts. The two dorsoventral corners of the LED arena were occluded from the fly's field of view
543 by the tethering stage [73]. Thus, a bar moving back to front on the display ipsilateral to the
544 recording site does not reach its full height for the first ~10° excursion. Schematic
545 representations of the visual stimuli in the figures are therefore depicted as trapezoids.

546 Visual stimuli were grouped into sets such that each set encompassed a single block of trials,
547 presented in random block design. To reduce onset artifacts, all motion stimuli included a 4
548 second pre- and post-stimulus epoch where the background illumination was set to 50% of the
549 maximum LED intensity. We waited at least 8 seconds between stimuli to allow cellular activity
550 to return to baseline. The arena was off throughout these inter-stimulus intervals. Visual
551 stimulus onset times were aligned to specific imaging frames by using voltage signals that
552 encoded pattern movement, position, and frame capture times (BNC-2090, National
553 Instruments, 10kHz sampling rate).

554 Visual stimulus parameters are listed below for each figure. In most experiments we used three
555 different types of stimuli that we refer to as standard stimuli: an 8.8°x8.8° dark object, an
556 8.8°x70° dark vertically elongated bar, and a grating projected across the entire display ('wide-
557 field') with a period of 17.6°. For these stimuli, the intensity of the background was always set to
558 50% of the maximum LED intensity, whereas the foreground figure (small object or bar) was
559 dark (0% intensity). For population imaging from axon terminals, each fly was presented with
560 three repetitions of each block, trials were averaged for analysis. For dendritic and single neurite
561 recordings, measurements were performed at different z-planes and each fly was presented
562 with a single stimulus block at each z-plane.

563 In most experiments, visual stimuli were presented in multiple directions. Back to front (ipsi- to
564 contralateral) and front to back (contra- to ipsilateral) responses were not statistically different
565 from each other. Therefore, unless otherwise noted, we presented front to back responses
566 (contra- to ipsilateral).

567 Weber Contrast (Figure 3B, B') was calculated using the following equation:

568
$$\text{Weber contrast} = \frac{I_{fg} - I_{bg}}{I_{bg}}$$

569 where I_{fg} is the light intensity of the foreground figure and I_{bg} the intensity of the background. In
570 our experiments the background intensity was always set to 50%, and a Weber contrast of -1
571 thus corresponds to 0% LED intensity (LEDs off) of the stimulus, whereas a Weber contrast of
572 +1 corresponds to 100% intensity.

573 Stimulus parameters:

574 **Figure 1D:** three types of contrast defined visual stimuli, 1. dark small object, 8.8×8.8° (width x
575 height), moving in the vertical center (equator) of the arena; 2. dark bar, 8.8×70°; 3. wide-field
576 grating, period: 17.6°. All patterns with I_{fg} = 0%, I_{bg} = 50%, movement direction: contra- to
577 ipsilateral, velocity: 22°/s.

578 **Figure 2D, 2E, 2F:** dark small object, 8.8×8.8°; dark bar, 8.8×70°; wide-field grating, period:
579 17.6°. I_{fg} =0%, I_{bg} = 50%, movement direction: contra- to ipsilateral, velocity: 22°/s.

580 **Figure 3A:** ON and OFF bar, 8.8×70°, Luminance: OFF bar, I_{fg} = 0%, I_{bg} = 50%; ON bar, I_{fg} =
581 100%, I_{bg} = 50%, movement direction: contra- to ipsilateral, velocity: 22°/s.

582 **Figure 3B:** bar, 8.8×70°, I_{fg} = 0-100% in 12.5% intervals, I_{bg} = 50%, movement direction:
583 contra- to ipsilateral, velocity: 44°/s.

584 **Figure 3C:** dark bar, 8.8×70°, I_{fg} = 0%, I_{bg} = 50%, stimulus was either presented as a static
585 flicker (bar appearing and disappearing at +26° position on the display) or moving with a
586 constant velocity of 44°/s from the contralateral to ipsilateral arena side.

587 **Figure 4C, 4D, 5A:** dark bar, two types: 2.2×66° for horizontal movements, 105×2.2° for vertical
588 movements, I_{fg} = 0%, I_{bg} = 50%, velocity: 22°/s, movement direction: up, down, left, right.

589 **Figure 5B, 5C:** dark bar, 8.8×70°, I_{fg} = 0%, I_{bg} = 50%, movement direction: contra- to
590 ipsilateral, stimulus velocity: 22, 44, 66, 88, 110, 132°/s.

591 **Figure 6A:** figure height varied and was 2.2, 4.4, 8.8, 17.6, 35, 52, or 70°. Figure width was 4.4°
592 in all conditions. I_{fg} = 0%, I_{bg} = 50%, movement direction: contra- to ipsilateral, velocity: 22°/s.

593 **Figure 6B:** figure width varied and was 2.2, 4.4, 8.8, 17.6, 35, or 70°. Figure height was 4.4° in
594 all conditions. I_{fg} = 0%, I_{bg} = 50%, movement direction: contra- to ipsilateral, velocity: 22°/s.

595 **Figure 6C:** two types of dark bars, 4.4×70° and 70×70°, I_{fg} = 0%, I_{bg} = 50%, movement
596 direction: contra- to ipsilateral, stimulus velocity: 22°/s.

597 **Figure 7A, 7B:** two types of stimuli, 1. dark bar, 8.8×70° moving across a stationary wide-field
598 grating, period 17.6°; 2. dark bar, 8.8×70° moving across a wide-field grating, period 17.6°. Both
599 stimuli with I_{fg} = 0%, I_{bg} = 25% for OFF grating and 50% for ON grating, movement direction:
600 contra- to ipsilateral, velocity: 44°/s.

601 **Figure 7C:** two types of stimuli, 1. dark small object, 8.8×8.8° moving across a stationary wide-
602 field grating, period 17.6°; 2. dark small object, 8.8×8.8° moving across a wide-field grating,
603 period 17.6°. Both stimuli with I_{fg} = 0%, I_{bg} = 25% for OFF grating and 50% for ON grating,
604 movement direction: contra- to ipsilateral, velocity: 44°/s.

605 **Figure S1A:** three types of motion defined visual stimuli, 1. randomly textured small object,
606 8.8×8.8°; 2. randomly textured bar, 8.8×70°; 3. randomly textured wide-field panorama. All
607 patterns with I_{fg} = 0%, I_{bg} = 50%, movement direction: contra- to ipsilateral, velocity: 22°/s.

608 **Figure S2:** Same as Fig 2D.

609 **Figure S3A:** dark bar, 8.8×70° moving across a wide-field grating, period 17.6°. I_{fg} = 0%, I_{bg} =
610 25% for OFF grating and 50% for ON grating, velocity: 0 or 44°/s for bar and background.
611 Conditions: 1. bar moving on stationary background, 2. bar and background moving from
612 contra- to ipsilateral, 3. bar and background moving from contra- to ipsilateral but background
613 starts to move with 3.36 s delay, 4. background only from contra- to ipsilateral, 5. bar moving
614 from contra- to ipsilateral and background moving from ipsi- to contralateral, 6. bar moving from
615 contra- to ipsilateral and background moving from ipsi- to contralateral but with 1.46 s delay, 7.
616 background only from ipsi- to contralateral.

617 **Figure S3B:** same as S3A but with a dark small object, 8.8×8.8°.

618 **Two-photon image analysis**

619 Calcium imaging data was analyzed offline using custom written MATLAB scripts. Images were
620 corrected for motion artifacts using a previously described algorithm [74]. Images that could not
621 be aligned or that contained persistent motion artifacts generated by the wriggling fly were
622 discarded. Aligned images were exported to MATLAB and ROI selection was in accord with the
623 anatomical region that was recorded. For every pixel in this ROI mask, mean and standard
624 deviation were calculated for the full time series. A test value for each pixel was calculated by
625 the product of mean and standard deviation of each pixel. Pixels with test values greater than or
626 equal to twice the mean value of all test values in the ROI mask were used for analysis. For
627 each stimulus condition, three trials were averaged, and $\Delta F/F$ was calculated by dividing the
628 signal by the mean intensity of the first 20 frames (2 s) preceding the stimulus motion onset.

629 **Receptive field size and directional selectivity**

630 To determine the functional RF size of LC12 and LC15 we measured integrated responses to a
631 2.2×66° wide dark bar (for left/right sweeps) and a 105×2.2° wide dark bar (for up/down
632 sweeps) moving within 13.2° spaced bins (Fig 4B'). The bar stimulus was moved in all four
633 cardinal directions (up, down, left, right) and the stimulus was presented only in the visible

634 regions of the display (-26.4° to +79.2° azimuth, -35° to +35° elevation). This area was divided
635 into eight horizontal bins (each 13.2° wide and 66° high) and five vertical bins (13.2° high, 105°
636 wide). Stimuli were moved within the boundaries of each bin in all four cardinal directions (left
637 and right in the horizontal bins, up and down in the vertical bins). During a sweep the bar
638 appeared at the start of the bin, was held stationary for 1 s before moving at 22°/s to the bin end
639 and disappeared. Calcium responses from individual LC12 and LC15 neurons were extracted
640 from single arbors in the lobula that showed no anatomical overlap to neighboring arbors. Only
641 flies where the anteroposterior plane did not change during all 26 experimental conditions were
642 included in the analysis. Neither LC12 nor LC15 showed directional selectivity in the horizontal
643 or vertical axis and response amplitudes to left and right bar movement and up and down bar
644 movement were almost identical. To assess the RF size, we averaged the left and right
645 movement responses of each bin, as well as up and down responses. The averaged time series
646 of each horizontal bin of individual neurites were multiplied with the averaged time series of
647 each vertical bin to derive the activity matrices in Figures 4C and 4D. RF sizes across neurites
648 showed little variation for both LC15 (~3x3 bins) and LC12 (1 bin). Maximum GCaMP6f
649 responses always occurred in the most centered bin, thus defined as the RF center (Fig 4C',
650 4D'). To determine the average RF size across animals, we spatially normalized to the bin that
651 showed the strongest calcium responses (bin 0 = RF center) and plotted the surrounding
652 responses relative to bin 0 (Figure 4C', D'). LC15 neurites with their RF occluded by the display
653 boundary were excluded from the analysis. Maximum GCaMP6f responses of all recorded
654 neurites were averaged for each normalized bin separately and plotted as a heat map (Fig 4C',
655 4D').

656 ***Anatomy and Immunohistochemistry***

657 *Dissection*

658 We followed standard *D. melanogaster* immunohistochemistry protocols [75]. In brief, flies were
659 dissected in PBS and dissection time never exceeded 10 minutes. Dissected brains were
660 placed in 4% paraformaldehyde diluted in PBS and fixed for 25 minutes at room temperature,
661 followed by washing with PBST (0.3% v/v Triton-X100) three times for 15 minutes each. Brains
662 were then incubated in PBST+5% normal goat serum (PBST-NGT) for 60 minutes at room
663 temperature and incubated in primary antibodies for 2 days at 4°C diluted in PBST-NGT. Brains
664 were then washed three times (PBST, 15 min each) and incubated with secondary antibodies
665 diluted in PBST-NGT for 2 days at 4°C. After three more washes (PBST, 15 min each) brains
666 were mounted on a microscope slide in Vectashield (Vector Labs, H-1000).

667 *LC anatomy labeling*

668 We used 3-5 days old female flies to visualize LC anatomy (Fig S1B) and the distribution of
669 presynaptic and postsynaptic sites in the lobula (Fig 2A). Primary antibodies were anti-
670 Bruchpilot (mouse monoclonal antibody Nc82, supernatant, Developmental Studies Hybridoma
671 Bank, 1:10 dilution), anti-DsRed rabbit polyclonal antibody (Takara, 632496, 1:200 dilution), and
672 anti-GFP chicken polyclonal antibody (abcam, 13970, 1:1000 dilution). Secondary antibodies
673 used were Alexa Fluor 488 goat anti-chicken (abcam, ab150169, 1:1000 dilution), Alexa Fluor
674 568 goat anti-rabbit (ThermoFisher Scientific, A-11036, 1:200 dilution), and Alexa Fluor 647
675 goat anti-mouse (ThermoFisher Scientific, A-21236, 1:200 dilution).

676 Multicolor stochastic labeling of individual neurons
677 MCFO-1 was used (Figure 4A) and expression patterns for GAL4 lines and/or presynaptic
678 marker distribution were performed as previously described using *pJFRC51-3xUAS-IVS-*
679 *syt::smHA(attp1)* and *pJFRC225-5xUAS-IVS-myc::smFP-FLAG (VK00005)* as reporters. Flies
680 were raised at 25°C and heat-shocked at 37°C for 10 min at mid-pupal stage. Eclosed flies were
681 dissected within three days and brains were stained following MCFO immunohistochemistry
682 protocol as described by Nern and colleagues [47]. Primary antibodies were anti-Bruchpilot
683 (mouse monoclonal antibody Nc82, supernatant, Developmental Studies Hybridoma Bank, 1:10
684 dilution) as a neuropil marker, rabbit anti-HA (Cell Signaling Technologies, 3724S, 1:300
685 dilution) and rat anti-FLAG (Novus Biologicals, NBP1-06712, 1:300 dilution). Secondary
686 antibodies used were Alexa Fluor 488 goat anti-rabbit (ThermoFisher Scientific, A-11008, 1:200
687 dilution), Alexa Fluor 594 goat anti-rat (Jackson ImmunoResearch Lab 112-585-167, 1:200
688 dilution), and Alexa Fluor 647 goat anti-mouse (ThermoFisher Scientific, A-21236, 1:200
689 dilution).

690 Image acquisition

691 Images were acquired with an LSM700 confocal microscope using a 40x oil immersion lens
692 (NA1.3, Zeiss). Z-stacks were acquired with a step size of 0.4-0.7 μm between optical sections.
693 Acquired images were visualized and processed offline using Fiji.

694 **QUANTIFICATION AND STATISTICAL ANALYSIS**

695 We used standard statistical tests to evaluate our data, and the results are reported at the
696 relevant locations in the figure captions. Statistics were computed in MATLAB with the Statistics
697 toolbox. Normal distribution of data sets was tested using the Kolmogorov-Smirnov (Lillifors) test
698 with a significance level of $p < 0.01$. All presented data were normally distributed and significant
699 differences were calculated using the paired-sample t-test or one-way ANOVA. Statistical test
700 results are reported in APA style (t-test: $t(\text{degrees of freedom}) = t \text{ value}, p = p \text{ value}$; one way
701 ANOVA: $F(\text{degrees of freedom}, \text{residual}) = F \text{ value}, p = p \text{ value}$). Significant differences are
702 stated as $*p < 0.05$, $**p < 0.01$, $***p < 0.001$. Data collection and analysis were not conducted blind
703 to the conditions of the experiments. N denotes the number of flies, while n refers to the number
704 recorded of neurites or individual cells. Final figures were prepared in Adobe Illustrator CS6.

705

706 **REFERENCES**

- 707 1. Lettvin, J., Maturana, H., McCulloch, W., and Pitts, W. (1959). What the Frog's Eye Tells
708 the Frog's Brain. Proc. IRE 47, 1940–1951.
- 709 2. Hubel, D.H., and Wiesel, T.N. (1965). Receptive fields and functional architecture in two
710 nonstriate visual areas (18 and 19) of the cat. J. Neurophysiol. 28, 229–89.
- 711 3. Hubel, D.H., and Wiesel, T.N. (1962). Receptive fields, binocular interaction and
712 functional architecture in the cat's visual cortex. J. Physiol. 160, 106–54.
- 713 4. Gale, S.D., and Murphy, G.J. (2014). Distinct Representation and Distribution of Visual
714 Information by Specific Cell Types in Mouse Superficial Superior Colliculus. J. Neurosci.
715 34, 13458–13471.
- 716 5. Gale, S.D., and Murphy, G.J. (2016). Active Dendritic Properties and Local Inhibitory

- 717 Input Enable Selectivity for Object Motion in Mouse Superior Colliculus Neurons. *J.*
718 *Neurosci.* 36, 9111–23.
- 719 6. Preuss, S.J., Trivedi, C.A., vom Berg-Maurer, C.M., Ryu, S., and Bollmann, J.H. (2014).
720 Classification of Object Size in Retinotectal Microcircuits. *Curr. Biol.* 24, 2376–2385.
- 721 7. Egelhaaf, M. (1985). On the neuronal basis of figure-ground discrimination by relative
722 motion in the visual system of the fly. II. Figure-detection cells, a new class of visual
723 interneurons. *Biol. Cybern.* 52, 195–209.
- 724 8. O'Carroll, D.C. (1993). Feature-detecting neurons in dragonflies. *Nature* 362, 541–543.
- 725 9. Nordström, K., and O'Carroll, D.C. (2006). Small object detection neurons in female
726 hoverflies. *Proceedings. Biol. Sci.* 273, 1211–6.
- 727 10. Barnett, P.D., Nordström, K., and O'Carroll, D.C. (2007). Retinotopic Organization of
728 Small-Field-Target-Detecting Neurons in the Insect Visual System. *Curr. Biol.* 17, 569–
729 578.
- 730 11. Keleş, M.F., and Frye, M.A. (2017). Object-Detecting Neurons in *Drosophila*. *Curr. Biol.*
731 27, 680–687.
- 732 12. Wu, M., Nern, A., Williamson, W.R., Morimoto, M.M., Reiser, M.B., Card, G.M., and
733 Rubin, G.M. (2016). Visual projection neurons in the *Drosophila* lobula link feature
734 detection to distinct behavioral programs. *Elife* 5, e21022.
- 735 13. Klapoetke, N.C., Nern, A., Peek, M.Y., Rogers, E.M., Breads, P., Rubin, G.M., Reiser,
736 M.B., and Card, G.M. (2017). Ultra-selective looming detection from radial motion
737 opponency. *Nature* 551, 237–241.
- 738 14. von Reyn, C.R., Nern, A., Williamson, W.R., Breads, P., Wu, M., Namiki, S., and Card,
739 G.M. (2017). Feature Integration Drives Probabilistic Behavior in the *Drosophila* Escape
740 Response. *Neuron* 94, 1190-1204.e6.
- 741 15. Silies, M., Gohl, D.M., and Clandinin, T.R. (2014). Motion-Detecting Circuits in Flies:
742 Coming into View. *Annu. Rev. Neurosci.* 37, 307–327.
- 743 16. Behnia, R., and Desplan, C. (2015). Visual circuits in flies: Beginning to see the whole
744 picture. *Curr. Opin. Neurobiol.* 34, 125–132.
- 745 17. Borst, A., Haag, J., and Reiff, D.F. (2010). Fly Motion Vision. *Annu. Rev. Neurosci.* 33,
746 49–70.
- 747 18. Borst, A., and Helmstaedter, M. (2015). Common circuit design in fly and mammalian
748 motion vision. *Nat. Neurosci.* 18, 1067–1076.
- 749 19. Jacob, S.N., and Nienborg, H. (2018). Monoaminergic Neuromodulation of Sensory
750 Processing. *Front. Neural Circuits* 12, 51.
- 751 20. Cheng, K.Y., and Frye, M.A. (2019). Neuromodulation of insect motion vision. *J. Comp.*
752 *Physiol. A*.
- 753 21. Hadjiconstantinou, M., and Neff, N.H. (1984). Catecholamine systems of retina: A model
754 for studying synaptic mechanisms. *Life Sci.* 35, 1135–1147.
- 755 22. Fischbach, K.F., and Dittrich, A.P.M. (1989). The optic lobe of *Drosophila melanogaster*.
756 I. A Golgi analysis of wild-type structure. *Cell Tissue Res.* 258, 441–475.
- 757 23. Otsuna, H., and Ito, K. (2006). Systematic analysis of the visual projection neurons of
758 *Drosophila melanogaster*. I. Lobula-specific pathways. *J. Comp. Neurol.* 497, 928–958.
- 759 24. Strausfeld, N.J., and Okamura, J.-Y. (2007). Visual system of calliphorid flies:
760 Organization of optic glomeruli and their lobula complex efferents. *J. Comp. Neurol.* 500,
761 166–188.
- 762 25. Panser, K., Tirian, L., Schulze, F., Villalba, S., Jefferis, G.S.X.E., Bühler, K., and Straw,

- 763 A.D. (2016). Automatic Segmentation of *Drosophila* Neural Compartments Using GAL4
764 Expression Data Reveals Novel Visual Pathways. *Curr. Biol.* 26, 1943–1954.
- 765 26. Mu, L., Ito, K., Bacon, J.P., and Strausfeld, N.J. (2012). Optic glomeruli and their inputs in
766 *Drosophila* share an organizational ground pattern with the antennal lobes. 32, 6061–71.
- 767 27. Aptekar, J.W., Keleş, M.F., Lu, P.M., Zolotova, N.M., and Frye, M.A. (2015). Neurons
768 Forming Optic Glomeruli Compute Figure–Ground Discriminations in *Drosophila*. *J.*
769 *Neurosci.* 35, 7587–99.
- 770 28. von Reyn, C.R., Breads, P., Peek, M.Y., Zheng, G.Z., Williamson, W.R., Yee, A.L.,
771 Leonardo, A., and Card, G.M. (2014). A spike-timing mechanism for action selection. *Nat.*
772 *Neurosci.* 17, 962–970.
- 773 29. Ribeiro, I.M.A., Drews, M., Bahl, A., Machacek, C., Borst, A., and Dickson, B.J. (2018).
774 Visual Projection Neurons Mediating Directed Courtship in *Drosophila*. *Cell* 174, 607-
775 621.e18.
- 776 30. Ache, J.M., Polsky, J., Alghailani, S., Parekh, R., Breads, P., Peek, M.Y., Bock, D.D., von
777 Reyn, C.R., and Card, G.M. (2019). Neural Basis for Looming Size and Velocity Encoding
778 in the *Drosophila* Giant Fiber Escape Pathway. *Curr. Biol.* 29, 1073-1081.e4.
- 779 31. Mongeau, J.M., Cheng, K.Y., Aptekar, J., and Frye, M.A. (2019). Visuomotor strategies
780 for object approach and aversion in *Drosophila melanogaster*. *J. Exp. Biol.* 222.
- 781 32. Van Breugel, F., and Dickinson, M.H. (2012). The visual control of landing and obstacle
782 avoidance in the fruit fly *Drosophila melanogaster*. *J. Exp. Biol.* 215, 1783–1798.
- 783 33. Maimon, G., Straw, A.D., and Dickinson, M.H. (2010). Active flight increases the gain of
784 visual motion processing in *Drosophila*. *Nat. Neurosci.* 13, 393–399.
- 785 34. Cheng, K.Y., Colbath, R.A., and Frye, M.A. (2019). Olfactory and Neuromodulatory
786 Signals Reverse Visual Object Avoidance to Approach in *Drosophila*. *Curr. Biol.* 29,
787 2058-2065.e2.
- 788 35. Mongeau, J.M., and Frye, M.A. (2017). *Drosophila* Spatiotemporally Integrates Visual
789 Signals to Control Saccades. *Curr. Biol.* 27, 2901-2914.e2.
- 790 36. Mronz, M., and Lehmann, F.O. (2008). The free-flight response of *Drosophila* to motion of
791 the visual environment. *J. Exp. Biol.* 211, 2026–2045.
- 792 37. Strother, J.A., Wu, S.T., Rogers, E.M., Eliason, J.L.M., Wong, A.M., Nern, A., and Reiser,
793 M.B. (2018). Behavioral state modulates the on visual motion pathway of *drosophila*.
794 *Proc. Natl. Acad. Sci. U. S. A.* 115, E102–E111.
- 795 38. Longden, K.D., and Krapp, H.G. (2010). Octopaminergic Modulation of Temporal
796 Frequency Coding in an Identified Optic Flow-Processing Interneuron. *Front. Syst.*
797 *Neurosci.* 4.
- 798 39. Suver, M.P., Mamiya, A., and Dickinson, M.H. (2012). Octopamine Neurons Mediate
799 Flight-Induced Modulation of Visual Processing in *Drosophila*. *Curr. Biol.* 22, 2294–2302.
- 800 40. Jenett, A., Rubin, G.M., Ngo, T.T.B., Shepherd, D., Murphy, C., Dionne, H., Pfeiffer, B.D.,
801 Cavallaro, A., Hall, D., Jeter, J., *et al.* (2012). A GAL4-Driver Line Resource for
802 *Drosophila* Neurobiology. *Cell Rep.* 2, 991–1001.
- 803 41. Keleş, M.F., Hardcastle, B.J., Städele, C., Qi, X., and Frye, M.A. (2020). Inhibitory
804 interactions and columnar inputs to an object motion detector in *Drosophila*. *Cell Rep.* *in*
805 *press*.
- 806 42. Schnell, B., Raghu, S.V., Nern, A., and Borst, A. (2012). Columnar cells necessary for
807 motion responses of wide-field visual interneurons in *Drosophila*. *J. Comp. Physiol. A*
808 198, 389–395.

- 809 43. Talay, M., Richman, E.B., Snell, N.J., Hartmann, G.G., Fisher, J.D., Sorkaç, A., Santoyo,
810 J.F., Chou-Freed, C., Nair, N., Johnson, M., *et al.* (2017). Transsynaptic Mapping of
811 Second-Order Taste Neurons in Flies by trans-Tango. *Neuron* 96, 783-795.e4.
- 812 44. Enell, L., Hamasaka, Y., Kolodziejczyk, A., and Nässel, D.R. (2007). γ -Aminobutyric acid
813 (GABA) signaling components in *Drosophila*: Immunocytochemical localization of GABA
814 B receptors in relation to the GABA A receptor subunit RDL and a vesicular GABA
815 transporter. *J. Comp. Neurol.* 505, 18–31.
- 816 45. Mauss, A.S., Meier, M., Serbe, E., and Borst, A. (2014). Optogenetic and pharmacologic
817 dissection of feedforward inhibition in *Drosophila* motion vision. *J. Neurosci.* 34, 2254–
818 2263.
- 819 46. Nicolai, L.J.J., Ramaekers, A., Raemaekers, T., Drozdzecki, A., Mauss, A.S., Yan, J.,
820 Landgraf, M., Annaert, W., Hassan, B.A., Nicolaï, L.J.J., *et al.* (2010). Genetically
821 encoded dendritic marker sheds light on neuronal connectivity in *Drosophila*. *Proc. Natl.*
822 *Acad. Sci.* 107, 20553–20558.
- 823 47. Nern, A., Pfeiffer, B.D., and Rubin, G.M. (2015). Optimized tools for multicolor stochastic
824 labeling reveal diverse stereotyped cell arrangements in the fly visual system. *Proc. Natl.*
825 *Acad. Sci. U. S. A.* 112, E2967-76.
- 826 48. Dhande, O.S., Stafford, B.K., Franke, K., El-Danaf, R., Percival, K.A., Phan, A.H., Li, P.,
827 Hansen, B.J., Nguyen, P.L., Berens, P., *et al.* (2019). Molecular fingerprinting of on–off
828 direction-selective retinal ganglion cells across species and relevance to primate visual
829 circuits. *J. Neurosci.* 39, 78–95.
- 830 49. Kim, T., Soto, F., and Kerschensteiner, D. (2015). An excitatory amacrine cell detects
831 object motion and provides feature-selective input to ganglion cells in the mouse retina.
832 *Elife* 4, e08025.
- 833 50. Ölveczky, B.P., Baccus, S.A., and Meister, M. (2003). Segregation of object and
834 background motion in the retina. *Nature* 423, 401–408.
- 835 51. Ache, J.M., Namiki, S., Lee, A., Branson, K., and Card, G.M. (2019). State-dependent
836 decoupling of sensory and motor circuits underlies behavioral flexibility in *Drosophila*.
837 *Nat. Neurosci.* 22, 1132–1139.
- 838 52. Evans, P.D., and Gee, J.D. (1980). Action of formamidine pesticides on octopamine
839 receptors. *Nature* 287, 60–62.
- 840 53. Behnia, R., Clark, D.A., Carter, A.G., Clandinin, T.R., and Desplan, C. (2014). Processing
841 properties of on and off pathways for *Drosophila* motion detection. *Nature* 512, 427–430.
- 842 54. Strother, J.A., Nern, A., and Reiser, M.B. (2014). Direct observation of on and off
843 pathways in the *drosophila* visual system. *Curr. Biol.* 24, 976–983.
- 844 55. Joesch, M., Schnell, B., Raghu, S.V., Reiff, D.F., and Borst, A. (2010). ON and off
845 pathways in *Drosophila* motion vision. *Nature* 468, 300–304.
- 846 56. Maisak, M.S., Haag, J., Ammer, G., Serbe, E., Meier, M., Leonhardt, A., Schilling, T.,
847 Bahl, A., Rubin, G.M., Nern, A., *et al.* (2013). A directional tuning map of *Drosophila*
848 elementary motion detectors. *Nature* 500, 212–216.
- 849 57. Wiederman, S.D., Shoemaker, P.A., and O'Carroll, D.C. (2008). A Model for the
850 Detection of Moving Targets in Visual Clutter Inspired by Insect Physiology. *PLoS One* 3,
851 e2784.
- 852 58. Wiederman, S.D., Fabian, J.M., Dunbier, J.R., and O'Carroll, D.C. (2017). A predictive
853 focus of gain modulation encodes target trajectories in insect vision. *Elife* 6, e26478.
- 854 59. Fisher, Y.E., Silies, M., and Clandinin, T.R. (2015). Orientation Selectivity Sharpens
855 Motion Detection in *Drosophila*. *Neuron* 88, 390–402.

- 856 60. Gruntman, E., Romani, S., and Reiser, M.B. (2018). Simple integration of fast excitation
857 and offset, delayed inhibition computes directional selectivity in *Drosophila*. *Nat.*
858 *Neurosci.* *21*, 250–257.
- 859 61. Nordström, K., Barnett, P.D., and O’Carroll, D.C. (2006). Insect Detection of Small
860 Targets Moving in Visual Clutter. *PLoS Biol.* *4*, e54.
- 861 62. Takemura, S. ya, Nern, A., Chklovskii, D.B., Scheffer, L.K., Rubin, G.M., and
862 Meinertzhagen, I.A. (2017). The comprehensive connectome of a neural substrate for
863 ‘ON’ motion detection in *Drosophila*. *Elife* *6*.
- 864 63. Haag, J., Mishra, A., and Borst, A. (2017). A common directional tuning mechanism of
865 *Drosophila* motion-sensing neurons in the ON and in the OFF pathway. *Elife* *6*, e29044.
- 866 64. Candy, D.J. (1978). The regulation of locust flight muscle metabolism by octopamine and
867 other compounds. *Insect Biochem.* *8*, 177–181.
- 868 65. Arenz, A., Drews, M.S., Richter, F.G., Ammer, G., and Borst, A. (2017). The Temporal
869 Tuning of the *Drosophila* Motion Detectors Is Determined by the Dynamics of Their Input
870 Elements. *Curr. Biol.* *27*, 929–944.
- 871 66. Strother, J.A., Wu, S.T., Wong, A.M., Nern, A., Rogers, E.M., Le, J.Q., Rubin, G.M., and
872 Reiser, M.B. (2017). The Emergence of Directional Selectivity in the Visual Motion
873 Pathway of *Drosophila*. *Neuron* *94*, 168-182.e10.
- 874 67. Geurten, B.R.H., Nordström, K., Sprayberry, J.D.H., Bolzon, D.M., and O’Carroll, D.C.
875 (2007). Neural mechanisms underlying target detection in a dragonfly centrifugal neuron.
876 *J. Exp. Biol.* *210*, 3277–3284.
- 877 68. Wiederman, S.D., and O’Carroll, D.C. (2011). Discrimination of features in natural scenes
878 by a dragonfly neuron. *J. Neurosci.* *31*, 7141–7144.
- 879 69. Luan, H., Peabody, N.C., Vinson, C.R.R., and White, B.H. (2006). Refined Spatial
880 Manipulation of Neuronal Function by Combinatorial Restriction of Transgene
881 Expression. *Neuron* *52*, 425–436.
- 882 70. Pfeiffer, B.D., Jenett, A., Hammonds, A.S., Ngo, T.T.B., Misra, S., Murphy, C., Scully, A.,
883 Carlson, J.W., Wan, K.H., Laverty, T.R., *et al.* (2008). Tools for neuroanatomy and
884 neurogenetics in *Drosophila*. *Proc. Natl. Acad. Sci. U. S. A.* *105*, 9715–9720.
- 885 71. Weir, P.T., and Dickinson, M.H. (2015). Functional divisions for visual processing in the
886 central brain of flying *Drosophila*. *Proc. Natl. Acad. Sci. U. S. A.* *112*, E5523–E5532.
- 887 72. Reiser, M.B., and Dickinson, M.H. (2008). A modular display system for insect behavioral
888 neuroscience. *J. Neurosci. Methods* *167*, 127–139.
- 889 73. Omoto, J.J., Keleş, M.F., Nguyen, B.-C.M., Bolanos, C., Lovick, J.K., Frye, M.A., and
890 Hartenstein, V. (2017). Visual Input to the *Drosophila* Central Complex by
891 Developmentally and Functionally Distinct Neuronal Populations. *Curr. Biol.* *27*, 1098–
892 1110.
- 893 74. Akin, O., and Zipursky, S.L. (2016). Frazzled promotes growth cone attachment at the
894 source of a Netrin gradient in the *Drosophila* visual system. *Elife* *5*, ;5:e20762.
- 895 75. Helfrich-Förster, C. (2007). Immunohistochemistry in *Drosophila*. In *Circadian Rhythms.*
896 *Methods in Molecular Biology*, E. Rosato, ed., pp. 533–547.

KEY RESOURCES TABLE

REAGENT or RESOURCE	SOURCE	IDENTIFIER
Antibodies		
anti-brp mouse monoclonal antibody	Developmental Studies Hybridoma Bank	Nc82 (supernatant) RRID:AB_2314866
anti-DsRed rabbit polyclonal antibody	Takara	632496, RRID:AB_10013483
anti-GFP chicken polyclonal antibody	abcam	ab13970, RRID:AB_300798
anti-HA rabbit monoclonal antibody	Cell Signaling Technologies	3724S, RRID:AB_1549585
anti-FLAG rat monoclonal antibody	Novus Biologicals	NBP1-06712 RRID: AB_1625981
Alexa Fluor 488, goat anti-chicken	abcam	ab150169, RRID:AB_2636803
Alexa Fluor 488, goat anti-rabbit	ThermoFisher Scientific	A-11008, RRID:AB_143165
Alexa Fluor 568, goat anti-rabbit	ThermoFisher Scientific	A-11036, RRID:AB_10563566
Alexa Fluor 594, goat anti-rat	Jackson Immuno Research Lab	112-585-167 RRID:AB_2338383
Alexa Fluor 647, goat anti-mouse	ThermoFisher Scientific	A-21236, RRID:AB_141725
Chemicals, Peptides, and Recombinant Proteins		
Chlordimeform	Sigma-Aldrich	31099; CAS: 6164-98-3
Experimental Models: Organisms/Strains		
LC4: <i>R47H03-p65.AD(attP40); R72E01-GAL4.DBD(attP2)</i> , driver line	Bloomington Drosophila Stock Center [12]	RRID:BDSC_68259 Janelia ID: SS00315
LC6: <i>R92B02-p65.AD(attP40); R41C07-GAL4.DBD(attP2)</i> , driver line	Bloomington Drosophila Stock Center [12]	RRID:BDSC_68247 Janelia ID: OL0077B
LC9: <i>VT032961-p65.AD(attP40); VT040569-GAL4.DBD(attP2)</i> , driver line	Bloomington Drosophila Stock Center [12]	RRID:BDSC_68342 Janelia ID: SS02651
LC10: <i>R35D04-p65.AD(attP40); R71E06.DBD(attP2)</i> , driver line	Bloomington Drosophila Stock Center [12]	RRID:BDSC_68378 Janelia ID: SS00938
LC11: <i>R22H02-p65.AD(attP40); R20G06-Gal4.DBD(attP2)</i> , driver line	Bloomington Drosophila Stock Center [12]	RRID:BDSC_68362 Janelia ID: OL0015B
LC12: <i>R35D04-p65.AD(attP40); R65B05-GAL4.DBD(attP2)</i> , driver line	Bloomington Drosophila Stock Center [12]	RRID:BDSC_68352 Janelia ID: OL0007B
LC12: <i>R35D04-p65.AD(attP40); R55F01-GAL4.DBD(attP2)</i> , driver line	Bloomington Drosophila Stock Center [12]	RRID:BDSC_68353 Janelia ID: OL0008B
LC13: <i>R14A11-p65.AD(attP40); R50C10-GAL4.DBD(attP2)</i> , driver line	Bloomington Drosophila Stock Center [12]	RRID:BDSC_68257 Janelia ID: OL0027B
LC15: <i>R26A03-p65.AD(attP40); R24A02-</i>	Bloomington	RRID:BDSC_68258

<i>GAL4.DBD(attP2)</i> , driver line	Drosophila Stock Center [12]	Janelia ID: OL0042B
LC16: <i>R26A03-p65.AD(attP40); R54A05-GAL4.DBD(attP2)</i> , driver line	Bloomington Drosophila Stock Center [12]	RRID:BDSC_68331 Janelia ID: OL0046B
LC17: <i>R21D03-p65.AD(attP40); [R65C12-GAL4.DBD(attP2)</i> , driver line	Bloomington Drosophila Stock Center [12]	RRID:BDSC_68356 Janelia ID: OL0005B
LC18: <i>R92B11-p65.AD(attP40); R82D11-GAL4.DBD(attP2)</i> , driver line	Bloomington Drosophila Stock Center [12]	RRID:BDSC_68358 Janelia ID: OL0010B
LC20: <i>R35B06-GAL4.DBD(attP2); R17A04-p65.AD(VK00027)</i> , driver line	Bloomington Drosophila Stock Center [12]	RRID:BDSC_68260 Janelia ID: SS00343
LC21: <i>R41C05-p65.AD(attP40); R55C04-GAL4.DBD(attP2)</i> , driver line	Bloomington Drosophila Stock Center [12]	RRID:BDSC_68330 Janelia ID: OL0045B
LC22: <i>R64G10-p65.AD(attP40); R35B06-GAL4.DBD(attP2)</i> , driver line	Bloomington Drosophila Stock Center [12]	RRID:BDSC_68357 Janelia ID: OL0001B
LC24: <i>VT038216-p65.AD(attP40); VT026477-GAL4.DBD(attP2)</i> , driver line	Bloomington Drosophila Stock Center [12]	RRID:BDSC_68340 Janelia ID: SS02638
LC25: <i>VT009792-p65.AD(attP40); VT002021-GAL4.DBD(attP2)</i> , driver line	Bloomington Drosophila Stock Center [12]	RRID:BDSC_68341 Janelia ID: SS02650
LC26: <i>VT007747-p65.AD(attP40); R85H06-GAL4.DBD(attP2)</i> , driver line	Bloomington Drosophila Stock Center [12]	RRID:BDSC_68333 Janelia ID: SS02445
LPLC1: <i>R64G09-p65.AD(attP40); R37H04-GAL4.DBD(attP2)</i> , driver line	Janelia Research Campus [12]	Janelia ID: OL0029B
LPLC2: <i>R19G02-p65.AD(attP40); R75G12-GAL4.DBD(attP2)</i> , driver line	Janelia Research Campus [12]	Janelia ID: OL0048B
Pan neuronal: <i>GMR57C10-GAL4(attP2)</i> , driver line	Bloomington Drosophila Stock Center	RRID:BDSC_39171
GFP: <i>10XUAS-IVS-mCD8::GFP(attP2)</i> , effector line	Bloomington Drosophila Stock Center	RRID:BDSC_32185
GCaMP: <i>20xUAS-IVS-GCaMP6f(attP40)</i> , effector line	Bloomington Drosophila Stock Center	RRID:BDSC_42747
sytGCaMP: <i>UAS-sytGCaMP6s(attP40)</i> , effector line	Bloomington Drosophila Stock Center	RRID:BDSC_64415
<i>UAS-DenMark; UAS-syt.eGFP</i> , effector line	Bloomington Drosophila Stock Center [46]	RRID:BDSC_33064
MCFO: <i>pBPhsFlp2::PEST (attP3); pJFRC201-10XUAS-FRT > STOP > FRT-myr::smGFP-HA (VK0005), pJFRC240-10XUAS-FRT > STOP > FRT-myr::smGFP-V5-THS-10XUAS-FRT > STOP > FRT-myr::smGFP-FLAG (su(Hw)attP1)</i> , effector line	Bloomington Drosophila Stock Center [47]	RRID:BDSC_64085
Software and Algorithms		

MATLAB R2019a	MathWorks	https://www.mathworks.com/
Adobe Illustrator CS6	Adobe Systems Inc.	RRID:SCR_010279 http://www.adobe.com/products/illustrator.html
Deposited Data	Mendeley Data	doi: 10.17632/ssgpb4wmh9.1
MATLAB analysis code	B. Hardcastle	https://github.com/bjhardcastle/SlidebookObj
Fiji	Rasband, W.S, national Institutes of Health	RRID:SCR_002285 http://fiji.sc
SlideBook6	Intelligent Imaging Innovations Inc. (3i)	RRID:SCR_014300 https://www.intelligent-imaging.com/slidebook

Figure 1

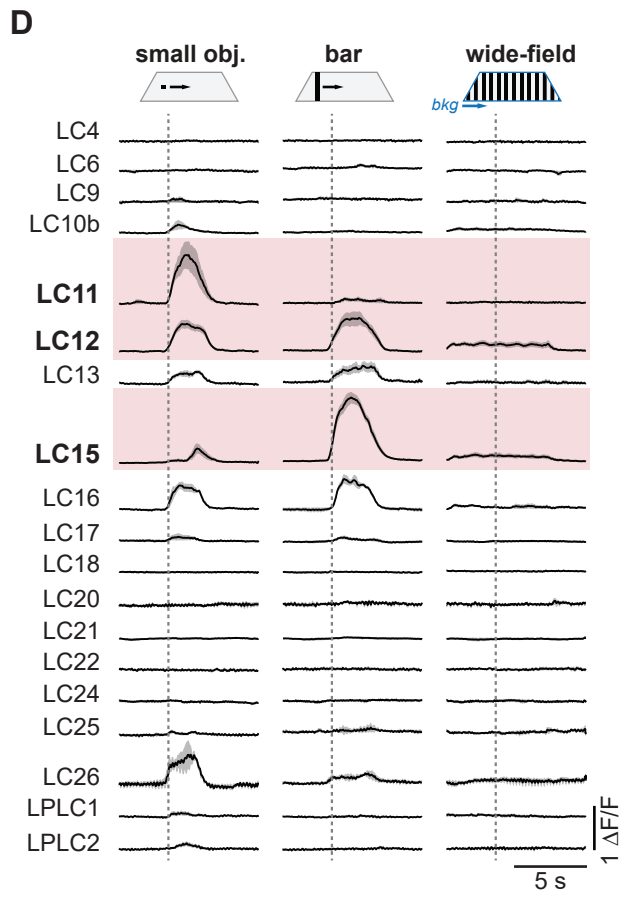
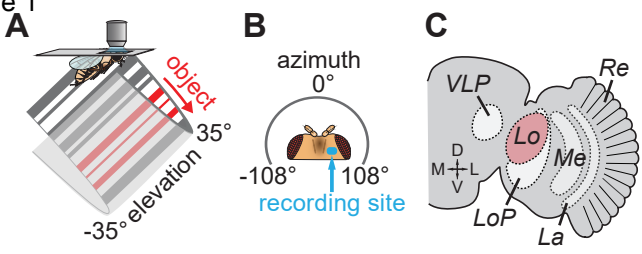


Figure 2

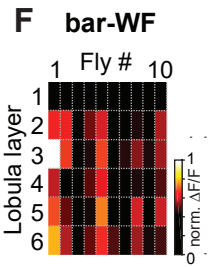
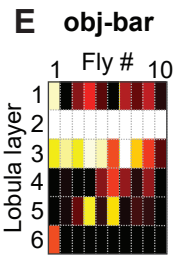
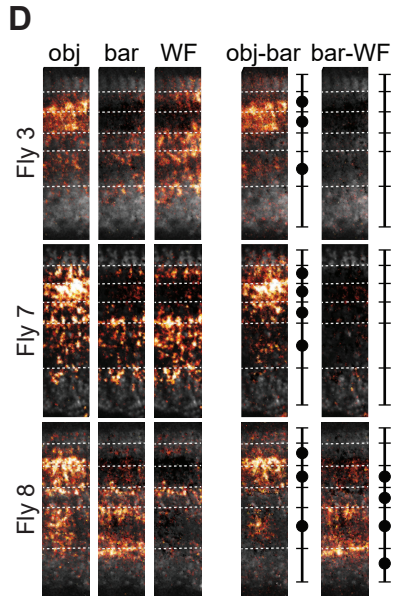
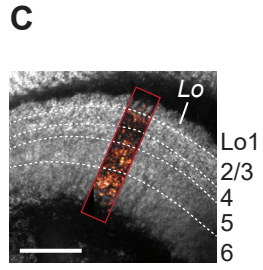
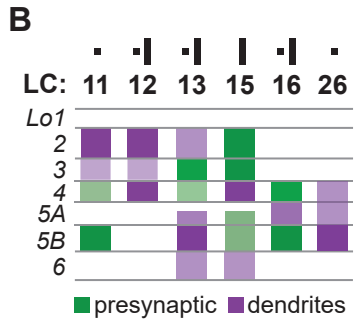
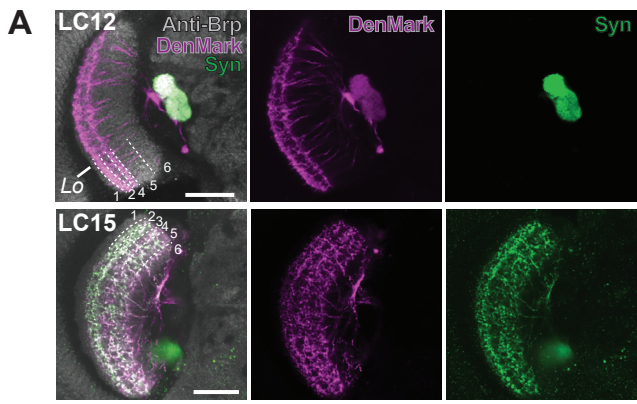


Figure 3

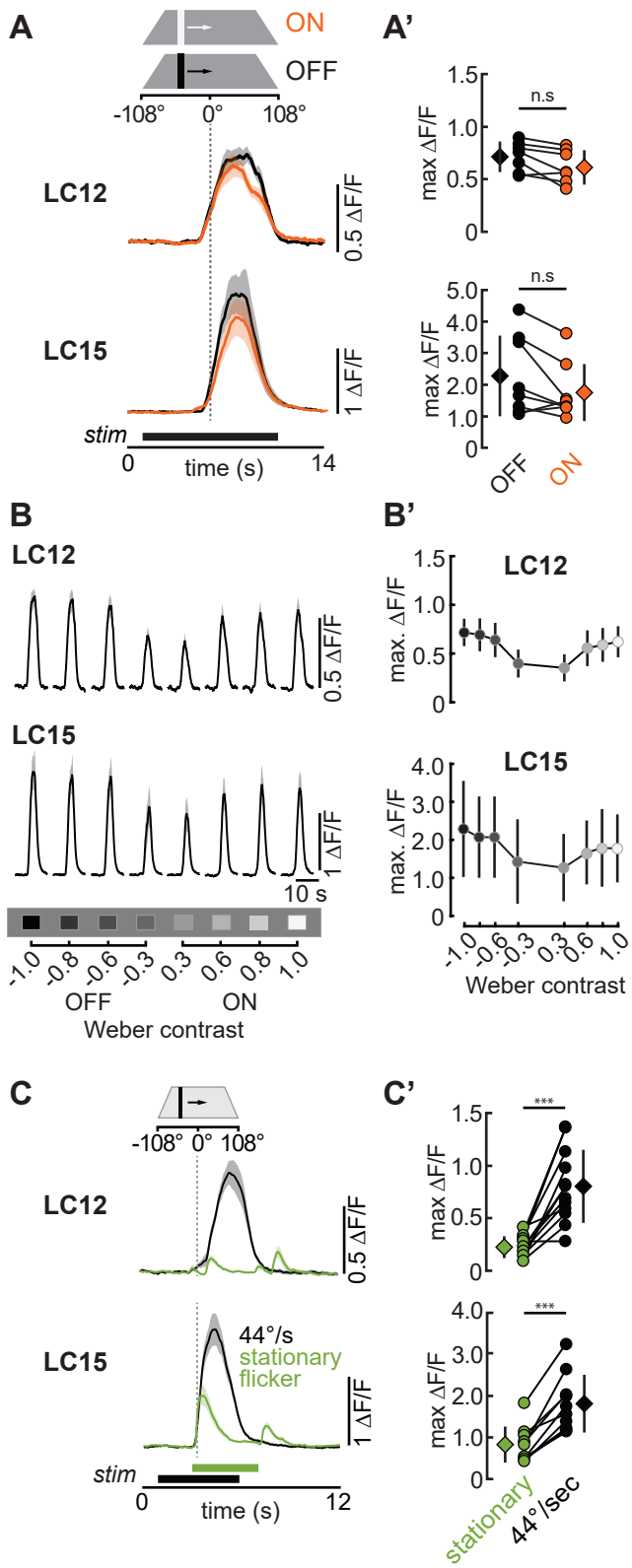


Figure 4

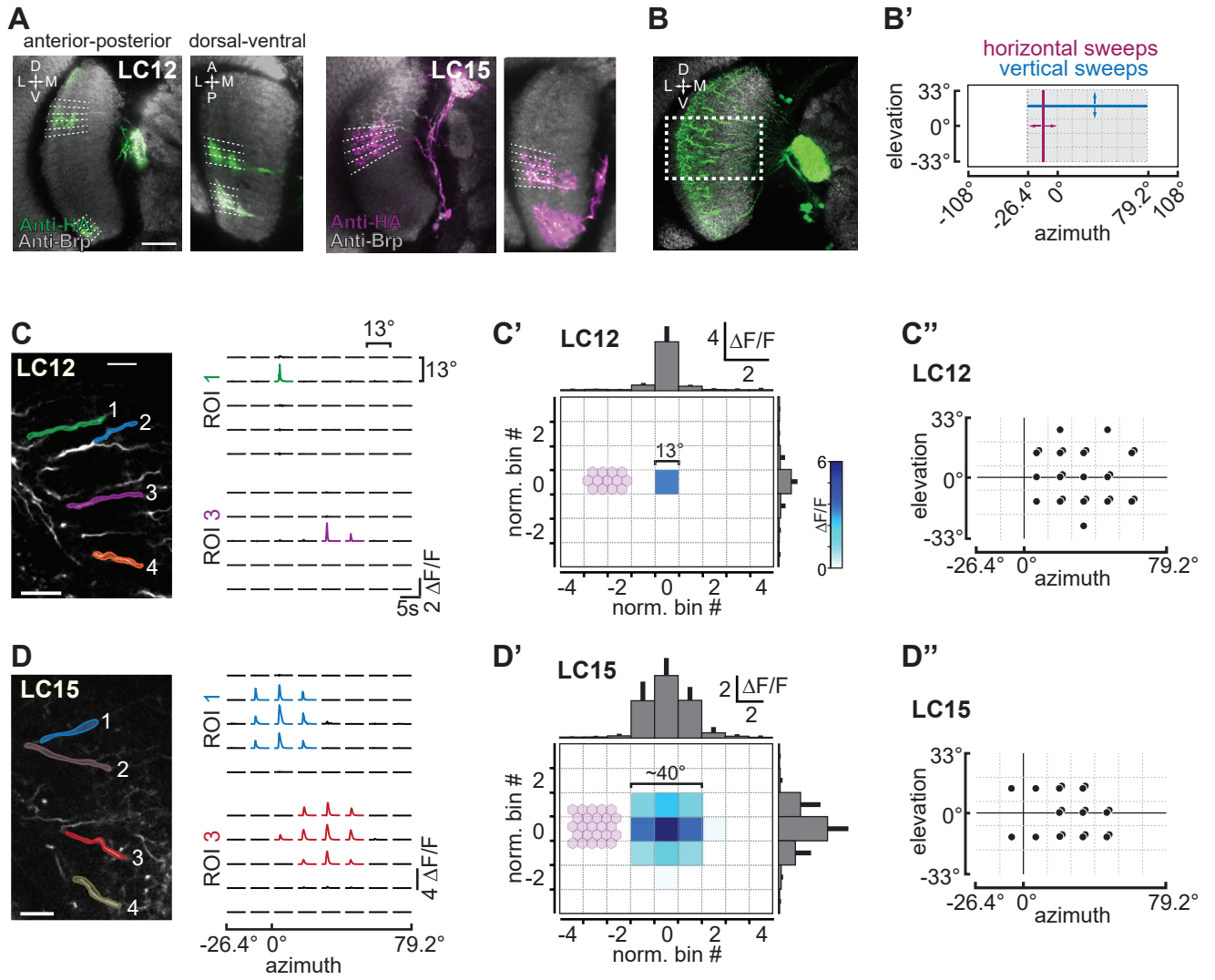


Figure 5

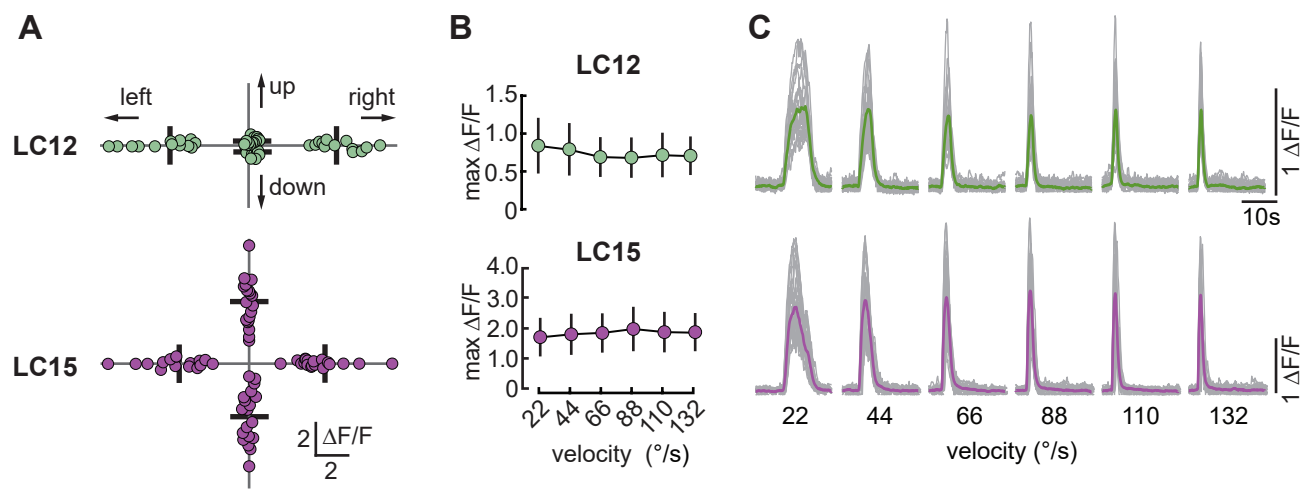


Figure 6

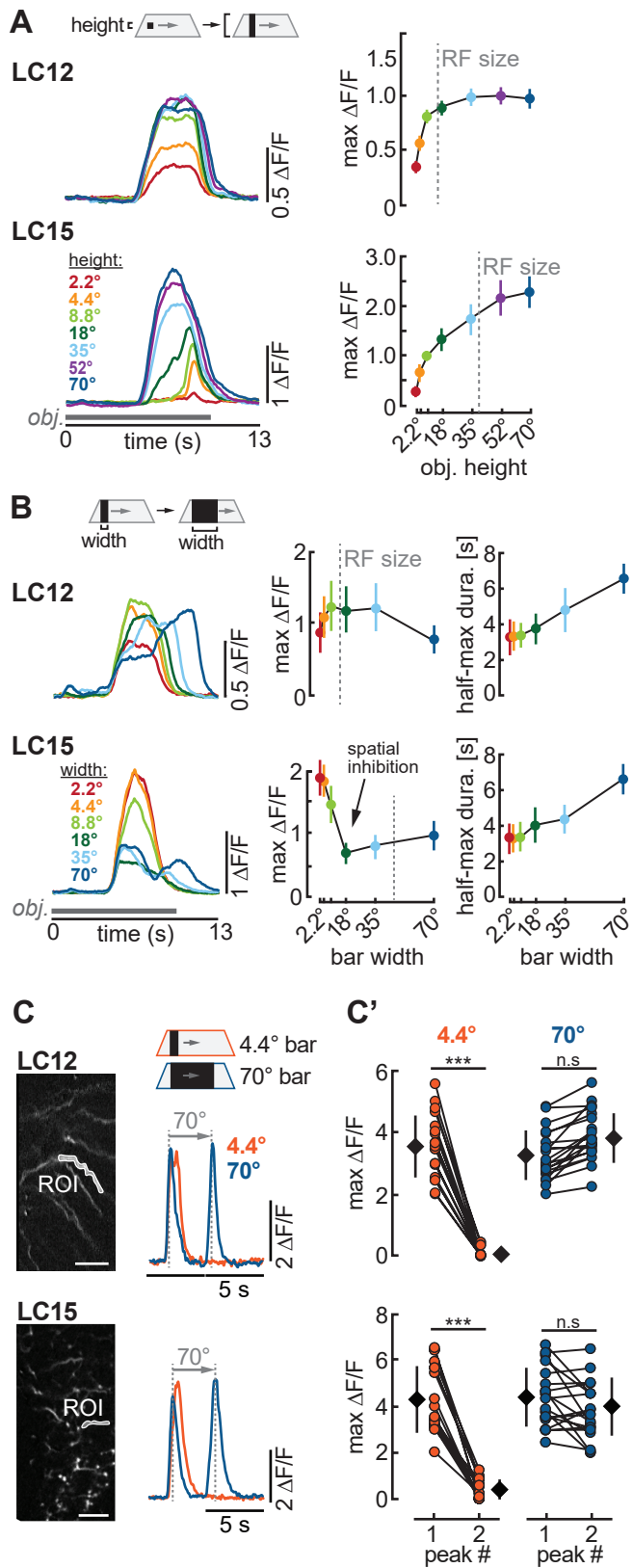
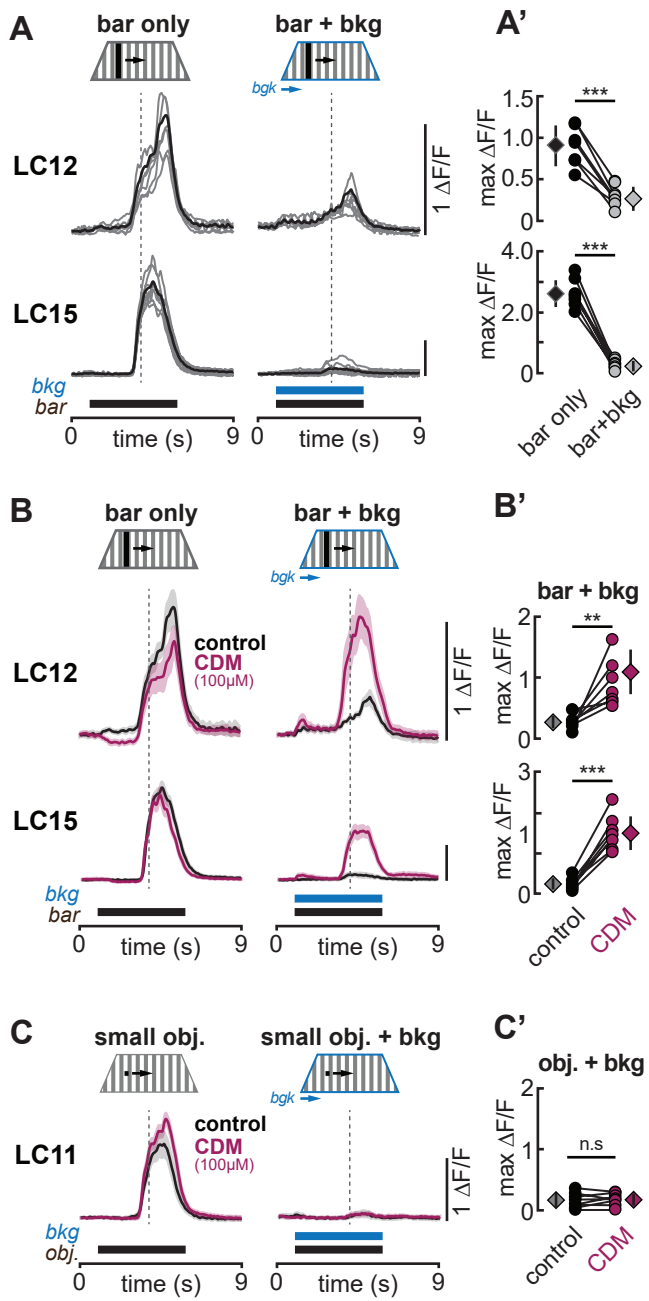


Figure 7



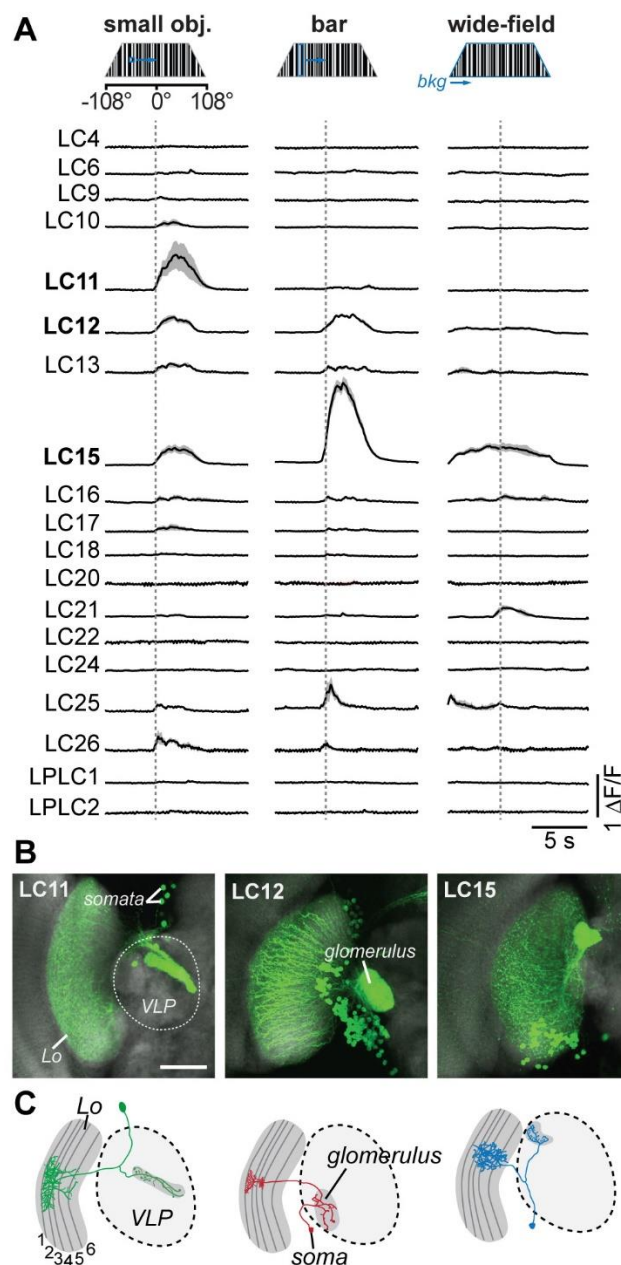


Figure S1. Lobula columnar neuron responses to motion defined visual stimuli. Related to Figure 1. (A) Mean glomerular GCaMP6f responses (\pm SD shading) of 19 LC neuron types to the movement of three types of motion defined visual stimuli: 1) $8.8 \times 8.8^\circ$ randomly textured small object, 2) a $8.8 \times 70^\circ$ randomly textured bar, 3) randomly textured wide-field grating. Visual stimuli are depicted at the top and moved from contra- to ipsilateral at $22^\circ/\text{s}$. Dashed lines indicate the time when visual stimuli passed the arena midline. $N =$ at least 5 flies for each LC type. **(B)** Anatomy of LC11, LC12, and LC15. Shown are maximum intensity projections of 10 slices ($0.46 \mu\text{m}$ step size) of the anterior view of flies expressing GFP (*UAS-mCD8::GFP*) in LC11, LC12, and LC15. Neuropil was labeled with anti-Bruchpilot antibody *nc82* (gray). Dashed line indicates the boundaries of the ventrolateral protocerebrum. Scale bar, $25 \mu\text{m}$. **(C)** Schematic of individual LC11, LC12, and LC15 neuron anatomy. Each LC neuron possesses arbors in different lobula layers and output terminals are concentrated into glomeruli in the ventrolateral protocerebrum. Re=retina, La=lamina, Me=medulla, LoP=lobula plate, Lo=Lobula, VLP= ventrolateral protocerebrum.

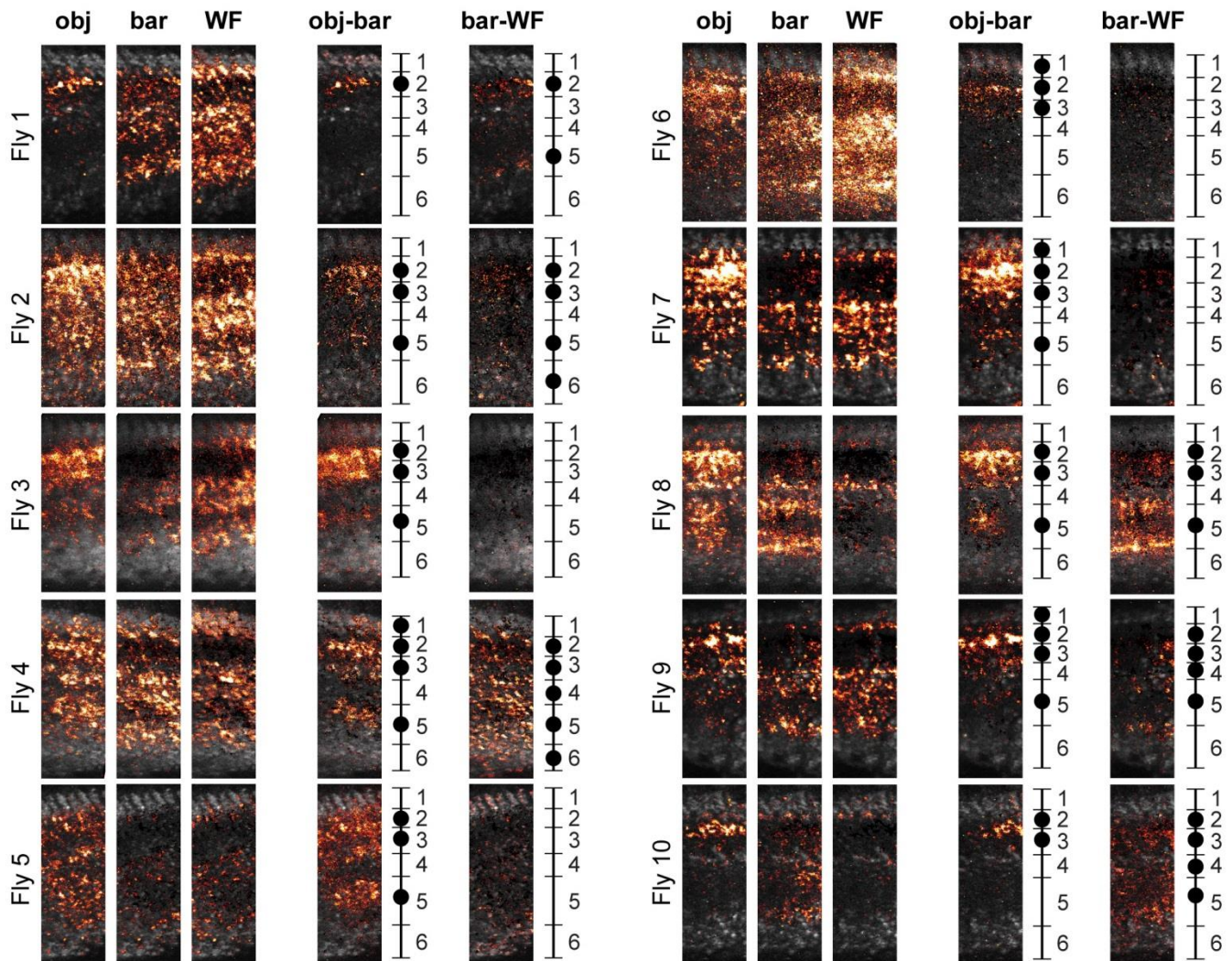


Figure S2. Layer specific input of small object information to lobula layer 2. Related to Figure 2. Mean activity images from two-photon calcium imaging experiments with sytGCaMP6s expressed in a pan neuronal driver (R57C10-GAL4) in response to a 8.8° square small object (obj), a $8.8 \times 70^\circ$ dark bar, and wide-field grating (WF, 17.6° period) of all ten tested flies. Schematics next to the mean activity images indicate innervated layers as filled circles. Obj-bar and bar-WF show subtracted mean calcium response of the corresponding visual stimuli.

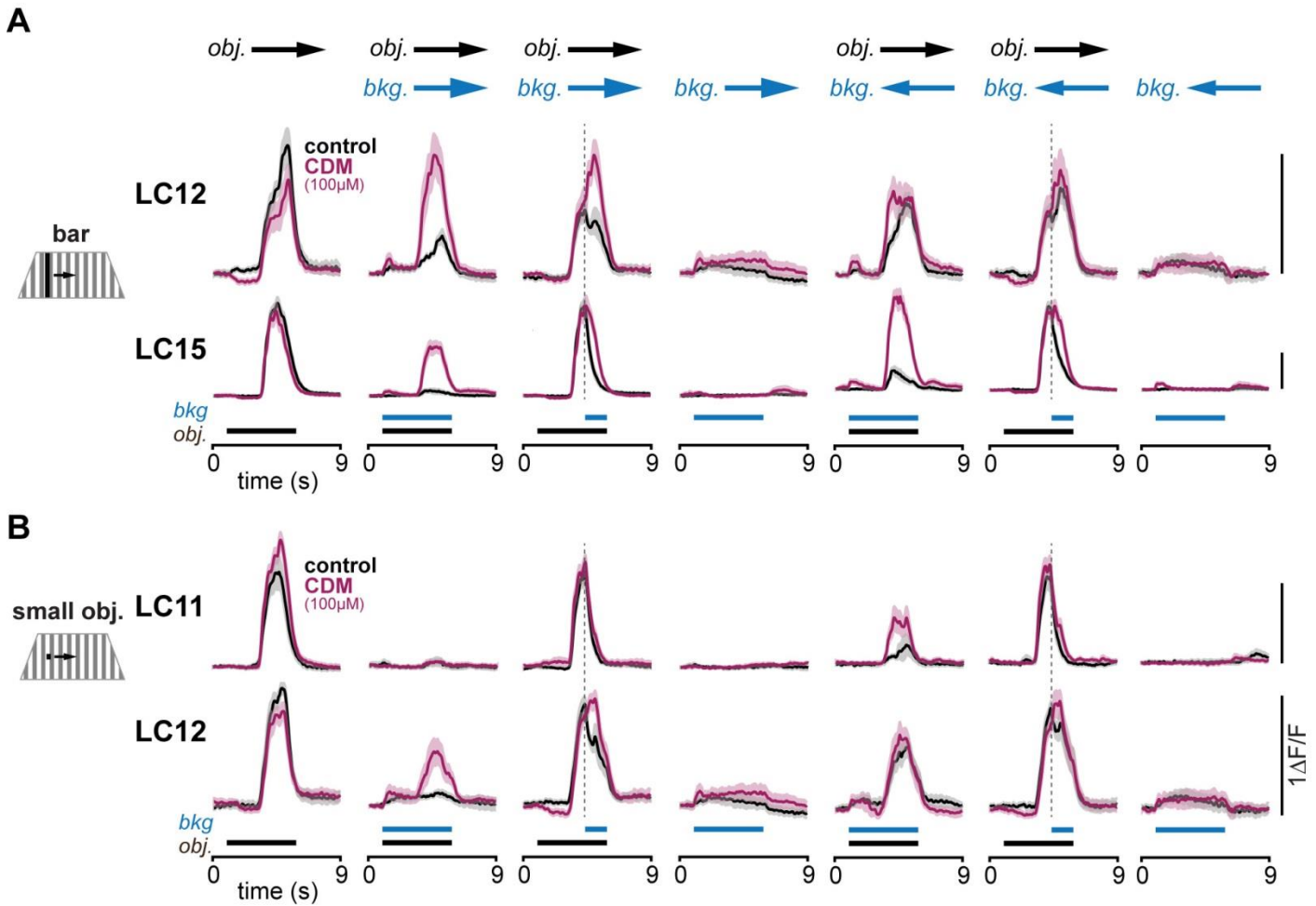


Figure S3. Octopaminergic neuromodulation of LC11, LC12, and LC15. Related to Figure 7. (A) Mean GCaMP6f responses (\pm SD shaded) for LC11 and LC12 to an $8.8 \times 8.8^\circ$ dark small object and (B) LC12 and LC15 to an $8.8 \times 70^\circ$ bar, both moving across a uniformly striped wide-field background grating. Arrows on top indicate the movement directions of the object (obj.) and the background (bkg.). Object and background movement time is indicated at the bottom. In conditions where the background movement started with a delayed onset, dashed lines were added to make potential effects on the calcium responses better visible. LC11: N=8 flies, LC12: N=7 flies, LC15: N=8 flies.

	LC12	LC15	Figure
contrast polarity	<u>contrast invariant</u> with equally strong responses to ON and OFF bar stimuli (N=7 flies)	<u>contrast invariant</u> with slightly stronger responses to OFF bar stimuli (N=8 flies)	3A, B'
object motion	<u>motion detector</u> minimal responses to flicker of repositioned objects (N=12 flies)	<u>motion detector</u> minimal responses to flicker of repositioned objects (N=10 flies)	3C
receptive field size	~13×13° (N=8 flies, n=26 neurites)	~40×40° (N=5 flies, n=20 neurites)	4C, D
dendritic span	~26×16° (anteroposterior: 5.2±1.2 columns, dorsoventral: 3.3±0.7 columns, N=9 flies, >50 cells)	~26×25° (anteroposterior: 5.3±0.6 columns, dorsoventral: 5.1±0.9 columns, N=11 flies, >50 cells)	4A, C', D'
directional selectivity	<u>horizontal motion detector</u> with no responses to vertical motion (N=8 flies, n=26 neurites)	<u>omni-directional motion detector</u> with equally strong responses in all four cardinal directions (N=5 flies, n=20 neurites)	5A
velocity tuning	<u>speed insensitive</u> (N=12 flies),	<u>speed insensitive</u> (N=10 flies)	5B, C
object height	<u>no height tuning</u> (N=9 flies)	<u>no height tuning</u> (N=10 flies)	6A
object width	<u>no width tuning</u> (N=9 flies)	<u>tuned to narrow width bars</u> ≤8.8° (N=9 flies)	6B

Table S1. Summary of LC12 and LC15 visual properties. Related to Figures 3-6.

Figure #	Genotype
<p>1D S1A</p>	<p>LC4: w[1118]; P{y[+t7.7] w[+mC]=R47H03-p65.AD}attP40/P{y[+t7.7] / w[+mC]=20XUAS-IVS-GCaMP6f}attP40; P{y[+t7.7] w[+mC]=R72E01-GAL4.DBD}attP2 / +.</p> <p>LC6: w[1118]; P{y[+t7.7] w[+mC]=R92B02-p65.AD}attP40 / w[+mC]=20XUAS-IVS-GCaMP6f}attP40; P{y[+t7.7] w[+mC]=R41C07-GAL4.DBD}attP2 / +.</p> <p>LC9: w[1118]; P{y[+t7.7] w[+mC]=VT032961-p65.AD}attP40 / w[+mC]=20XUAS-IVS-GCaMP6f}attP40; P{y[+t7.7] w[+mC]=VT040569-GAL4.DBD}attP2 / +.</p> <p>LC10: w[1118]; P{y[+t7.7] w[+mC]=R35D04-p65.AD}attP40 / w[+mC]=20XUAS-IVS-GCaMP6f}attP40; P{y[+t7.7] w[+mC]=R71E06-GAL4.DBD}attP2 / +.</p> <p>LC11: w[1118]; P{y[+t7.7] w[+mC]=R22H02-p65.AD}attP40 / w[+mC]=20XUAS-IVS-GCaMP6f}attP40; P{y[+t7.7] w[+mC]=R20G06-GAL4.DBD}attP2 / +.</p> <p>LC12: w[1118]; P{y[+t7.7] w[+mC]=R35D04-p65.AD}attP40 / w[+mC]=20XUAS-IVS-GCaMP6f}attP40; P{y[+t7.7] w[+mC]=R65B05-GAL4.DBD}attP2 / +.</p> <p>LC13: w[1118]; P{y[+t7.7] w[+mC]=R14A11-p65.AD}attP40 / w[+mC]=20XUAS-IVS-GCaMP6f}attP40; P{y[+t7.7] w[+mC]=R50C10-GAL4.DBD}attP2 / +.</p> <p>LC15: w[1118]; P{y[+t7.7] w[+mC]=R26A03-p65.AD}attP40 / w[+mC]=20XUAS-IVS-GCaMP6f}attP40; P{y[+t7.7] w[+mC]=R24A02-GAL4.DBD}attP2 / +.</p> <p>LC16: w[1118]; P{y[+t7.7] w[+mC]=R26A03-p65.AD}attP40 / w[+mC]=20XUAS-IVS-GCaMP6f}attP40; P{y[+t7.7] w[+mC]=R54A05-GAL4.DBD}attP2 / +.</p> <p>LC17: w[1118]; P{y[+t7.7] w[+mC]=R21D03-p65.AD}attP40 / w[+mC]=20XUAS-IVS-GCaMP6f}attP40; P{y[+t7.7] w[+mC]=R65C12-GAL4.DBD}attP2 / +.</p> <p>LC18: w[1118]; P{y[+t7.7] w[+mC]=R92B11-p65.AD}attP40 / w[+mC]=20XUAS-IVS-GCaMP6f}attP40; P{y[+t7.7] w[+mC]=R82D11-GAL4.DBD}attP2 / +.</p> <p>LC20: w[1118]; P{y[+t7.7] w[+mC]=R35B06-GAL4.DBD}attP2 / w[+mC]=20XUAS-IVS-GCaMP6f}attP40; w[+mC]=R17A04-p65.AD}VK00027 / +.</p> <p>LC22: w[1118]; P{y[+t7.7] w[+mC]=R64G10-p65.AD}attP40 / w[+mC]=20XUAS-IVS-GCaMP6f}attP40; P{y[+t7.7] w[+mC]=R35B06-GAL4.DBD}attP2 / +.</p> <p>LC24: w[1118]; P{y[+t7.7] w[+mC]=VT038216-p65.AD}attP40 / w[+mC]=20XUAS-IVS-GCaMP6f}attP40; P{y[+t7.7] w[+mC]=VT026477-GAL4.DBD}attP2 / +.</p> <p>LC25: w[1118]; P{y[+t7.7] w[+mC]=VT009792-p65.AD}attP40 / w[+mC]=20XUAS-IVS-GCaMP6f}attP40; P{y[+t7.7] w[+mC]=VT002021-GAL4.DBD}attP2 / +.</p> <p>LC26: w[1118]; P{y[+t7.7] w[+mC]=VT007747-p65.AD}attP40 / w[+mC]=20XUAS-IVS-GCaMP6f}attP40; P{y[+t7.7] w[+mC]=R85H06-GAL4.DBD}attP2 / +.</p> <p>LPLC1: w[1118]; P{y[+t7.7] w[+mC]=R64G09-p.65.AD}attP40 / w[+mC]=20XUAS-IVS-GCaMP6f}attP40; P{y[+t7.7] w[+mC]=R37H04-GAL4.DBD}attP2 / +.</p> <p>LPLC2: w[1118]; P{y[+t7.7] w[+mC]=R19G02-p.65.AD}attP40 / w[+mC]=20XUAS-IVS-GCaMP6f}attP40; P{y[+t7.7] w[+mC]=R75G12-GAL4.DBD}attP2 / +.</p>
<p>2A</p>	<p>LC12: w[1118]; P{w[+mC]=UAS-DenMark}2, P{w[+mC]=UAS-syt.eGFP}2 / P{y[+t7.7] w[+mC]=R35D04-p65.AD}attP40; In(3L)D, mirr[SaiD1] D[1]/TM6C, Sb[1] / P{y[+t7.7] w[+mC]=R65B05-GAL4.DBD}attP2.</p> <p>LC15: w[1118]; P{w[+mC]=UAS-DenMark}2, P{w[+mC]=UAS-syt.eGFP}2 / P{y[+t7.7] w[+mC]=R26A03-p65.AD}attP40; In(3L)D, mirr[SaiD1] D[1]/TM6C, Sb[1] / P{y[+t7.7]</p>

Figure #	Genotype
	w[+mC]=R24A02-GAL4.DBD}attP2.
2C 2D-F S2	w[*] / w[1118]; P{y[+t7.7] w[+mC]=UAS-sytGCaMP6s}attP40 / +; P{y[+t7.7] w[+mC]=GMR57C10-GAL4}attP2 / TM6B, Tb[1].
3A-C 3C-D 4C-D'' 5A-C 6A-C 7A-B S4A	LC12: w[1118]; P{y[+t7.7] w[+mC]=R35D04-p65.AD}attP40 / w[+mC]=20XUAS-IVS-GCaMP6f}attP40; P{y[+t7.7] w[+mC]=R65B05-GAL4.DBD}attP2 / +. LC15: w[1118]; P{y[+t7.7] w[+mC]=R26A03-p65.AD}attP40 / w[+mC]=20XUAS-IVS-GCaMP6f}attP40; P{y[+t7.7] w[+mC]=R24A02-GAL4.DBD}attP2 / +.
4A	LC12: w[1118] P{y[+t7.7] w[+mC]=hs-FLPG5.PEST}attP3 / w[1118]; P{y[+t7.7] w[+mC]=R35D04-p65.AD}attP40; PBac{y[+mDint2] w[+mC]=10xUAS(FRT.stop)myr::smGdP-HA}VK00005 P{y[+t7.7] w[+mC]=10xUAS(FRT.stop)myr::smGdP-V5-THS-10xUAS(FRT.stop)myr::smGdP-FLAG}su(Hw)attP1 / P{y[+t7.7] w[+mC]=R65B05-GAL4.DBD}attP2. LC15: w[1118] P{y[+t7.7] w[+mC]=hs-FLPG5.PEST}attP3 / w[1118]; P{y[+t7.7] w[+mC]=R26A03-p65.AD}attP40; PBac{y[+mDint2] w[+mC]=10xUAS(FRT.stop)myr::smGdP-HA}VK00005 P{y[+t7.7] w[+mC]=10xUAS(FRT.stop)myr::smGdP-V5-THS-10xUAS(FRT.stop)myr::smGdP-FLAG}su(Hw)attP1 / P{y[+t7.7] w[+mC]=R24A02-GAL4.DBD}attP2.
4B	LC12: w[1118] / w[*]; P{y[+t7.7] w[+mC]=R35D04-p65.AD}attP40; P{y[+t7.7] w[+mC]=R55F01-GAL4.DBD}attP2 / P{y[+t7.7] w[+mC]=10XUAS-IVS-mCD8::GFP}attP2.
7C	LC11: w[1118]; P{y[+t7.7] w[+mC]=R22H02-p65.AD}attP40 / w[+mC]=20XUAS-IVS-GCaMP6f}attP40; P{y[+t7.7] w[+mC]=R20G06-GAL4.DBD}attP2 / +.
S1B	LC11: w[1118] / w[*]; P{y[+t7.7] w[+mC]=R22H02-p65.AD}attP40; P{y[+t7.7] w[+mC]=R20G06-GAL4.DBD}attP2 / P{y[+t7.7] w[+mC]=10XUAS-IVS-mCD8::GFP}attP2. LC12: w[1118] / w[*]; P{y[+t7.7] w[+mC]=R35D04-p65.AD}attP40; P{y[+t7.7] w[+mC]=R55F01-GAL4.DBD}attP2 / P{y[+t7.7] w[+mC]=10XUAS-IVS-mCD8::GFP}attP2. LC15: w[1118] / w[*]; P{y[+t7.7] w[+mC]=R26A03-p65.AD}attP40; P{y[+t7.7] w[+mC]=R24A02-GAL4.DBD}attP2 / P{y[+t7.7] w[+mC]=10XUAS-IVS-mCD8::GFP}attP2.
S4B	LC11: w[1118]; P{y[+t7.7] w[+mC]=R22H02-p65.AD}attP40 / w[+mC]=20XUAS-IVS-GCaMP6f}attP40; P{y[+t7.7] w[+mC]=R20G06-GAL4.DBD}attP2 / +. LC12: w[1118]; P{y[+t7.7] w[+mC]=R35D04-p65.AD}attP40 / w[+mC]=20XUAS-IVS-GCaMP6f}attP40; P{y[+t7.7] w[+mC]=R65B05-GAL4.DBD}attP2 / +.

Table S2. Fly strains and genotypes, sorted by Figure number. Related to Star Methods.